DEVELOPMENT OF CRACK CHARACTERIZATION METHODOLOGY USING DIGITAL IMAGE CORRELATION

By

Landon Parker Dellenbaugh

Submitted to the graduate degree program in Civil, Environmental, and Architectural Engineering and the Graduate Faculty of the University of Kansas in partial fulfillment of the requirements for the degree of Master of Science.

_____

Chairperson William Collins

_____

Caroline Bennett

_____

Jian Li

Defense Date: January 29, 2021

Lawrence, Kansas

Keywords: Fatigue; Cracking; Bridge; Steel; Inspection; Digital Image Correlation

The thesis committee for Landon Parker Dellenbaugh certifies that this is the approved version of the following thesis:

DEVELOPMENT OF CRACK CHARACTERIZATION METHODOLOGY USING DIGITAL IMAGE CORRELATION

_____

Chairperson William Collins

_____

Caroline Bennett

_____

Jian Li

Approved Date: January 29, 2021

Abstract

Distortion-induced fatigue cracking is a primary maintenance and structural safety concern in steel bridges built prior to the 1980s in the United States. Manual, hands-on inspections are currently the primary method departments of transportation and other bridge owners use to identify and quantify fatigue cracks. To improve the efficacy of fatigue crack inspections, previous research has proposed and examined numerous fatigue crack detection approaches, including both user-implemented technology and structural health monitoring methods. However, these approaches typically require human presence and active participation at the location of interest, or prolonged mechanical contact and continuous monitoring of the structure. This limits the effectiveness and flexibility of these approaches for inspecting the large number of fatigue susceptible regions found on steel bridges. Recently, vision-based sensing technologies have been explored for applications related to damage detection and health assessment in civil infrastructure, as they offer the benefits of being low cost, non-contact, and deployable without human presence at the specific region of interest. This paper presents a digital image correlation-based methodology developed from in-plane compact fracture specimens for the detection and quantification of fatigue cracks. The effectiveness of the proposed methodology is further evaluated through experimental tests of a fatigue crack on a large-scale steel girder to cross-frame connection, similar to the out-of-plane fatigue cracks commonly found on steel highway bridges. Results indicate that the digital image correlation methodology can adequately characterize fatigue cracks, both in-plane and out-of-plane, in terms of crack length. This quantification from a non-contact inspection technology has the potential to lead to future automation of steel highway bridge fatigue inspections.

Acknowledgements

I would like to acknowledge everyone in the Department of Civil, Environmental, and Architectural Engineering at the University of Kansas with whom I have had the pleasure of working with over my time in the graduate program. Countless lifelong friendships have blossomed from my time at the University of Kansas and for that I am grateful.

I would especially like to express my gratitude towards Dr. William Collins for his mentorship throughout my graduate studies. This not only includes research guidance but also academic and life guidance as well. Also, I would like to thank my remaining committee members for their contributions and great advice: Dr. Caroline Bennett and Dr. Jian Li. I would like to thank Dr. Matt Fadden for his guidance for using the Digital Image Correlation equipment. Lab technicians David Woody and Kent Dye were instrumental in completing all laboratory tests and I am grateful for their outstanding support and hard work.

I would like to thank my fellow graduate students with whom I have spent countless hours over my time in graduate school including: Hunter Senior, Chase Breckwoldt, Hayder Al-Salih, Zahra Andalib, Tristan Yount, Duncan MacLachlan, Xiang-Xiong Kong, Kien Nguyen, Danqing Yu, and many others not listed here.

I would like to thank Dr. David Parr for his mentorship throughout my undergraduate degree that eventually led me to pursue my graduate degree at The University of Kansas.

Finally, I would like to thank my friends and family. Without their unwavering support none of this would have been possible.

TABLE OF CONTENTS

TABLE OF FIGURES

TABLE OF TABLES

Chapter 1: Project Overview and Thesis Organization

This report presents the work that investigated the performance of digital image correlation (DIC) technology, specifically focusing on steel highway bridge connections. Funded by the Mid-American Transportation Center, this research is focused on developing an automated bridge inspection methodology that will reduce the number of required hands-on inspections needed to meet federal requirements by replacing them with inspections performed using DIC.

Two different of laboratory tests of steel specimens were performed as part of this study. These two types of tests performed differed in their loading complexity. The first utilized the cyclic in-plane loading mode of compact (C(T)) specimens. These tests were performed to develop a series of algorithms that will process images of a specimen subjected to load to detect the presence of fatigue cracks. If cracks are present in the specimen, the length of the crack can also be calculated. The second test was performed on a half-scale model bridge cross-frame connection. This connection was chosen due to its nature of producing distortion induced fatigue cracks in the web-gap region. The methodology developed from the C(T) specimens was then tested at multiple load ranges to determine the range of applicability.

This thesis includes a reformatted journal article that has been accepted for publication in the American Society of Civil Engineer's Journal of Bridge Engineering. Also included in this thesis are Appendices A and B which present the data obtained from the test programs presented herein.

Chapter 2: Introduction

Bridges serve a critical role in maintaining many vital functions of modern society, but due to repetitive loads and long service lives they are prone to damage and deterioration. A recent report issued by the American Society of Civil Engineers assigned U.S. bridges a grade of C+, with over 9 percent of the inventory considered to be structurally deficient (ASCE 2017). For these structures to perform as needed up to and beyond their intended service lives, it is clear that they must be properly maintained and rehabilitated.

One of the biggest structural concerns to many aging steel bridges in the United States is the initiation and propagation of fatigue cracks (Fisher 1984). Caused by cyclic traffic loading, fatigue cracks are initially very small and often difficult to detect through visual inspection. However, if cracks go undetected and are allowed to propagate to critical size, fatigue cracking can compromise the structural integrity of an entire bridge putting human lives at risk. The majority of these cracks occur in the web-gap region between flanges and transverse stiffeners or connections plates, as shown in Figure 1. These distortion-induced fatigue cracks are caused by differential vertical movement between adjacent longitudinal girders resulting from the transverse placement of traffic loading. Due to design practices of the era, distortion-induced fatigue cracks are commonly found in steel U.S. bridges built prior to the 1980s (Zhao and Roddis 2004).

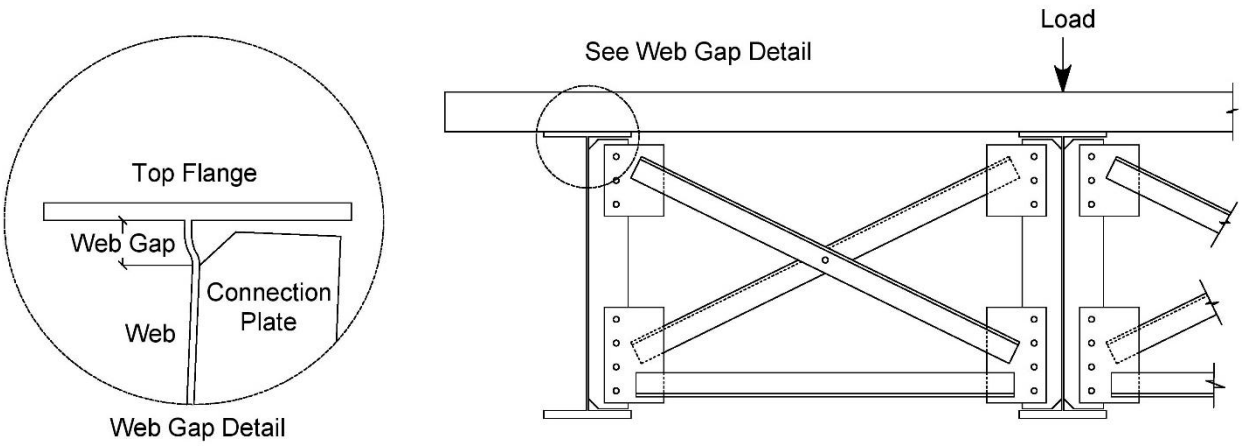

Figure 1. Distortion-induced fatigue mechanism.

Visual inspection is the most common approach for fatigue crack detection on steel bridges. Inspected on either a 24-month or 48-month cycle (FHWA 2004), fatigue damage in steel bridges is intended to be identified and monitored over time, with repairs made prior to cracks reaching critical size. In practice, however, visual inspections for fatigue cracks present a number of challenges. In addition to a low probability of detection, visual inspections are labor intensive, costly, and dangerous for inspectors and the traveling public (Whitehead 2015; Zhao and Haldar 1996).

Efforts to improve the efficacy of fatigue crack inspections through detection and monitoring have been undertaken in both the structural health monitoring (SHM) and non-destructive testing (NDT) research communities. A variety of sensing technologies have shown promise in detecting and monitoring cracks, both those induced by in-plane and out-of-plane fatigue loading. However, the majority of these approaches rely on sensors that are physically attached to the monitored structure. This reliance on discretized physical attachment limits the ability to efficiently and cost-effectively monitor a large number of fatigue susceptible regions on a structure. Vision-based, non-contact sensing technologies overcome these limitations, allowing

technologies to be deployed over large areas of a given structure. While numerous vision-based crack detection and characterization methods are described in the literature, the majority of studies have been conducted under idealized conditions examining in-plane fatigue loading or cracks in non-metallic materials (Vanlanduit et al. 2009; Rupil et al. 2011; Nowell et al. 2010). Very few have examined fatigue cracks in steel structures loaded through a realistic distortion-induced mechanism that commonly occurs in geometrically-complex steel bridge connections. The present work helps fill this gap by offering the results and analysis of a vision-based, non-contact fatigue crack evaluation on a steel bridge system under realistic loading conditions.

Chapter 3: Digital Image Correlation Background and Application

Digital image correlation (DIC) is a vision-based technology which uses image analysis software to produce full-field surface displacement and strain measurements. DIC requires a randomly-applied high contrast surface pattern, and compares a series of images collected while the surface deforms. Resulting digital images are discretized into small groups of pixels, known as subsets, and changes in gray scale in each subset are correlated with material surface displacements. DIC-based measurement approaches have previously been evaluated and applied in the context of civil infrastructure. An overview of relevant work is presented in the following, organized by applications to in-plane measurements, out-of-plane measurements, and fatigue crack characterization.

3.1 In-Plane Measurements

DIC has been used in previous studies to evaluate the in-plane displacement measurement of target surfaces on a variety of civil infrastructure. One of the primary applications of DIC is in measuring the deflection of critical bridge members under service loads. Pan et al. (2016) combined DIC and an inverse compositional algorithm to measure bridge deflection through digital videos. The proposed method was validated through in-service testing of a railway bridge. Dhanasekar et al. (2018) investigated the serviceability deflections of two historic masonry arch bridges under operating conditions using an advanced DIC system. Similar work was performed by Cigada et al. (2014) and Alipour et al. (2019). Despite the successful applications of these studies, some challenges to field deployment have been identified, including lighting conditions

(Ribeiro et al. 2014) and limitations on the distance between the camera and the material surface (Lee & Shinozuka 2006).

3.2 Out-of-Plane Measurements

When equipped with multiple cameras, DIC can be an effective tool to measure out-of-plane displacements. Chen et al. (2013) achieved accurate solutions when using a four-camera test setup to measure out-of-plane displacements, albeit sacrificing experimental configuration flexibility and ease of calibration due to test setup complexity. Helfrick et al. (2011) used a stereoscopic camera setup with a high-speed shutter to measure full-field out-of-plane vibrations, noting significant image resolution tradeoffs with camera speed. In an effort to examine the performance of DIC in complex loading scenarios, Sutton et al. (2007) developed clevis fixtures allowing for mixed-mode loading of compact (C(T)) specimens. Displacement results obtained from DIC were found to be in good agreement with those obtained from a 3D finite element model of the region surrounding the crack for Mode I opening and Mode II in-plane shear loading.

3.3 Fatigue Crack Detection and Characterization

Extensive research has been performed regarding the applicability of using DIC to detect and identify fatigue cracks in metallic materials under controlled laboratory settings. Previous studies have primarily examined fatigue cracks under in-plane, Mode I, loading conditions, attempting to either identify or characterize crack conditions. Recent studies in which DIC has been applied in this in-plane loading context include tests of aluminum channels (Vanlanduit et al. 2009) as well as steel C(T) specimens (Rupil et al. 2011; Nowell et al. 2010), tension plates with center-drilled bolt holes (Lorenzino et al. 2014; Hutt and Cawley 2009), and notched tension

specimens (Carrol et al. 2009; Carrol et al. 2013). DIC methods have also shown promise as an approach to experimentally determine stress intensity factors (Zhang & He 2012; Hamam et al. 2007).

These studies have been foundational in understanding the capabilities and limitations of DIC with respect to crack detection. Prior studies have resulted in qualitative identification and characterization of cracks. However, automated methodologies are still urgently needed to quantitatively evaluate cracks in in-service bridges. Furthermore, the effectiveness of DIC for detecting and quantifying cracking under out-of-plane fatigue loading conditions resulting in mixed-mode cracking has not been thoroughly researched. Researchers have postulated that this lack of experimental evaluation is potentially due to the inherent complexity and sophistication required for the out-of-plane test setups (Sutton et al. 2007).

Chapter 4: Objective and Scope

The objective of this study was to investigate the effectiveness and limitations of DIC when applied to the problem of distortion-induced fatigue cracks in steel bridges, working towards the development of a crack detection methodology robust enough to assist with and eventually serve as a potential replacement to human-based visual inspections. A quantifiable approach to out-of-plane fatigue characterization using DIC is required before this overarching long-term goal can be realized. This study presents a methodology that can be applied to detect fatigue cracks and quantify crack lengths under in-plane and distortion-induced fatigue loading. The methodology was first developed using in-plane fatigue specimens and was then evaluated using a bridge component specimen tested under realistic out-of-plane fatigue loading. Development of this methodology is intended to lay the groundwork for future research aimed at developing automatable systems capable of crack detection and characterization on in-service structures.

Chapter 5: Overall Experimental Approach

The methodology presented in this study was (1) developed through tests performed using DIC applied to in-plane C(T) specimens, and (2) validated through tests performed using DIC applied to a bridge component specimen subjected to distortion-induced fatigue. In the in-plane loading development stage, C(T) specimens were cyclically loaded to initiate and propagate Mode I fatigue cracks, where crack propagation was paused at discrete intervals of experimentally-known crack lengths and documented using DIC. DIC data was collected and evaluated for multiple load ranges at each increment of crack length. Vision-based algorithms were then applied and data analysis procedures developed to identify the crack path and the crack tip location, allowing for the calculation of crack length from DIC data.

Next, a half-scale bridge girder-to-cross-frame connection specimen was used to evaluate the methodology's effectiveness for detection of distortion-induced fatigue cracking. The cross-frame connection simulated both the geometry and out-of-plane loading conditions commonly found on steel bridges. The girder specimen was cycled under out-of-plane loading until fatigue cracking initiated in the web-gap region. The developed methodology was then applied to the girder specimen to detect and characterize the fatigue crack on this geometrically-complex test setup. The following sections present the methodology development, corresponding testing conditions, and validation.

Chapter 6: In-Plane Fatigue Crack

6.1 In-Plane Test Specimen Description

The initial testing was performed on steel C(T) specimens loaded in a uniaxial servo-hydraulic load frame. These tests were performed to develop the crack length quantification methodology in an idealized test environment with a simple specimen geometry for later application to the complex out-of-plane geometry. The C(T) specimen was 6.4-mm (0.25-in.) thick with a width of 127 mm (5.0 in.), allowing for the possibility of long cracks. In typical fatigue and fracture mechanics testing crack length is defined from the load line, which for a C(T) specimen is at the centerline of the loading pins, to the crack tip. However, this length includes a portion of the machined notch, a geometric feature that does not exist on bridge components. In the context of using DIC to identify and characterize a fatigue crack, a different convention is more applicable. In this study, all crack lengths on C(T) specimens were measured from the tip of the notch where fatigue crack initiation occurred, as shown in Figure 2.

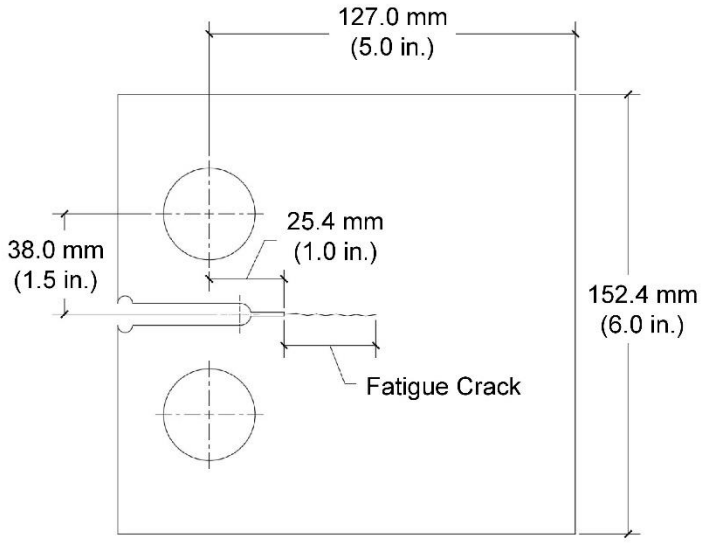

Figure 2. C(T) specimen dimensions.

6.2 In-Plane Loading Protocol

Truck loading on highway bridges is highly variable, so a fatigue crack inspection methodology needs to function over a range of load magnitudes. To evaluate the effectiveness of DIC in identifying and characterizing fatigue cracks, a loading protocol was developed to examine a range of realistic load scenarios. Crack propagation was conducted at low levels of stress intensity to avoid the influence of excessive crack tip plasticity, and to represent realistic cracks in steel bridge infrastructure. Five load cases, designated C(T)-LC1 through C(T)-LC5, were defined by applied stress intensity ranges (ΔK_I) of 11, 22, 33, 44, and 55 MPa$\sqrt{m}$ (10, 20, 30, 40, and 50 ksi$\sqrt{in}$), as shown in Table 1. Each load case used an *R*-ratio, the ratio of minimum to maximum load, of 0.1. All load cases were examined at each of four crack lengths ranging from 12.7 to 50.8 mm (0.5 to 2.0 in.), in 12.7-mm (0.5-in.) long increments. All stress intensity-based load calculations and corresponding crack length measurements were computed based on compliance equations validated and accepted for the given specimen geometry (ASTM 2018). For each crack length, crack tip plasticity was limited during testing by applying the lowest loading range, C(T)-LC1, first and increasing to the highest, C(T)-LC5. Once testing was concluded for each crack length, crack growth was reinitiated at a low stress intensity range and the crack was propagated to the next desired increment of crack length, ensuring crack extension beyond any previously-induced plastic zone.

Table 1. Convergence of in-plane specimens for multiple crack lengths

Load Case	Stress Intensity Factor Range, ΔKI MPa√m (ksi√in)	Crack Length mm (in.)			
		12.7 (0.5)	25.4 (1.0)	38.1 (1.5)	50.8 (2.0)
C(T)-LC1	11 (10)	90.9%	98.3%	98.9%	99.3%
C(T)-LC2	22 (20)	67.6%	94.7%	99.6%	99.3%
C(T)-LC3	33 (30)	86.7%	92.9%	89.9%	99.7%
C(T)-LC4	44 (40)	68.5%	85.8%	94.8%	97.7%
C(T)-LC5	55 (50)	61.5%	91.2%	91.4%	95.0%

6.3 In-Plane DIC Configuration

The in-plane DIC tests performed on C(T) specimens were conducted using a single camera setup, consistent with the 2D testing approach, as shown in Figure 3. The PGR Grasshopper3 camera used a Sony IMX250 complementary metal oxide semiconductor (CMOS) sensor and was equipped with a 17 mm (0.67 in.) lens and mounted on an adjustable tripod. Details of cameras, lenses, and lighting sources can be found in Table 2. External adjustable LED lighting panels were used to eliminate shadows induced by ambient laboratory lighting as well as to provide the necessary contrast for data analysis. High contrast was applied to the specimen by coating the surface with white paint and then applying black spray paint in a random, speckle pattern. Black speckle sizes ranged from approximately 0.5 to 2.5 mm^2 (0.0007 to 0.04 $in.^2$), and covered about one third of the specimen surface. System calibration was performed prior to testing with a calibration plate provided by the system manufacturer, Correlated Solutions (Irmo, South Carolina). Conditions were examined prior to each test with a noise study, and system resolution was typically on the order of 0.0003 mm (0.00001 in.) or better. Analysis of the collected images utilized Correlated Solutions' VIC-2D software with a subset size of 29 pixels and a step size of 7

pixels. These values were automatically calculated within the software. Post-processing performed within the DIC analysis software was limited to coordinate transformation, aligning the y-axis to the direction of the load line and the x-axis to the crack path, as denoted in Figure 4.

Table 2. Camera, lens, and lighting details

Equipment	Description	Specification
Camera	Model	PGR Grasshopper3
	Sensor	Sony IMX250 CMOS
	Resolution (megapixels)	5
	Resolution (horizontal x vertical) (pixels)	2,448 x 2,048
	Frame Rate (frame/s)	75
Lens	Model	Schneider Xenoplan
	Focal Length (mm)	17
	Iris range/ aperture	f1.4
Light	Model	Light Emitting Diode (LED) 500k Bescor lighting system

6.4 Development of Crack Characterization Methodology

Methods of interpreting DIC data, typically examined in terms of displacement or calculated strain, vary between researchers, but generally still require some operator visual identification. While the crack location was readily visually identifiable from either strain or displacement data in this case, as observable in Figure 4, automation of an inspection tool requires utilization of algorithms independent of operator interaction.

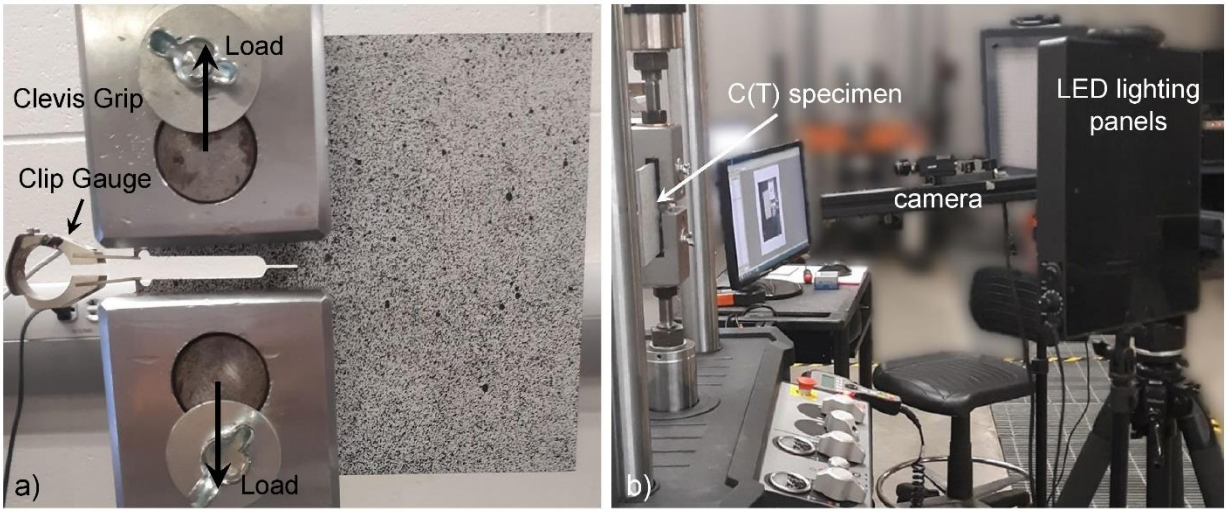

Figure 3. (a) C(T) specimen with high-contrast surface pattern; and (b) DIC hardware placement.

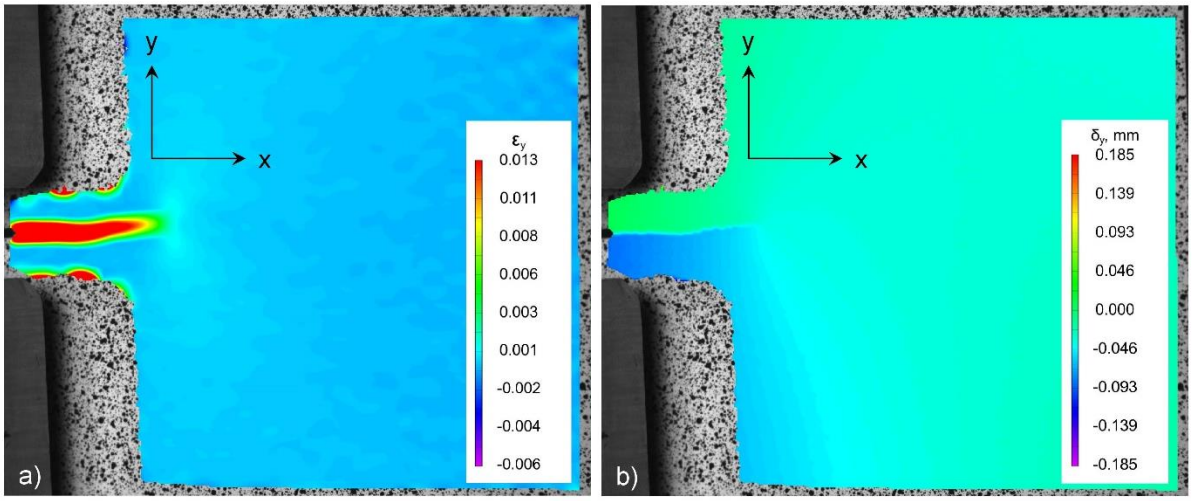

Figure 4. Typical visualized DIC results of the in-plane specimen in terms of the *y*-direction: (a) strain; and (b) displacement.

Although DIC results for strain produced images where the crack could be visualized, allowing for a qualitative understanding of behavior around fatigue cracks, exact geometric localization of the crack from this data proved difficult due to erroneously large strain values

calculated at the free edges of the crack surfaces during opening. As DIC algorithms calculate surface displacements over an entire subset of pixels, the extremely large strains calculated for crack faces spread beyond the exact location of the crack surfaces, making localization difficult. Displacement data do not have this issue, and are thus more suitable for crack localization. As will be illustrated in the following sections, an edge detection algorithm can identify the general crack path with high accuracy using the displacement image, offering a great advantage in future automation of this methodology, while achieving the same result with the strain image would be challenging. For this reason, only displacement-based DIC data were used in the present study. The methodology used to determine crack length from DIC data is schematically illustrated in Figure 5.

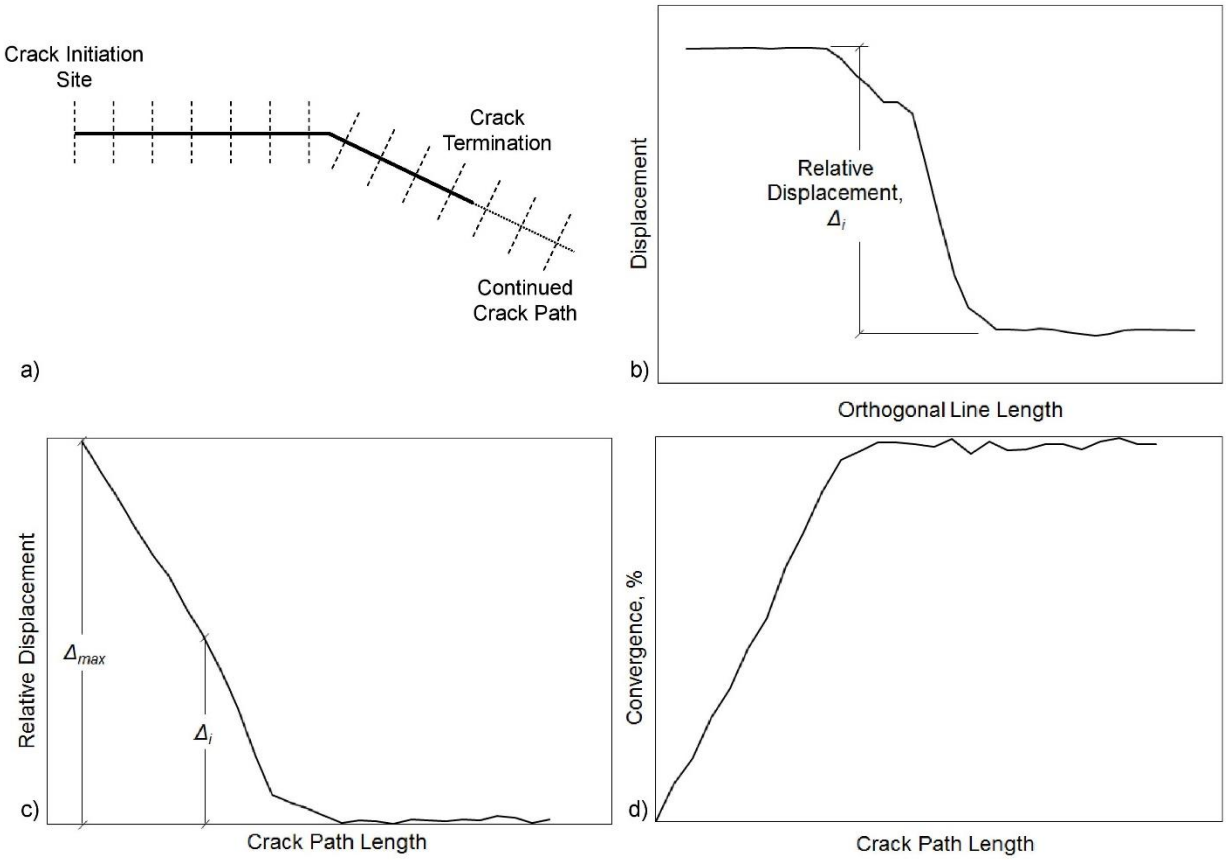

Figure 5. (a) Crack path and data export lines; (b) displacement values along a data export line; (c) relative displacement along the crack path; and (d) convergence along the crack path.

To initially identify the crack path, a matrix of y-axis displacement contours corresponding to the direction of crack opening was imported into MATLAB (MathWorks, Natick, Massachusetts) from the DIC analysis software. A basic Sobel edge detection algorithm (Parker 2011) was applied to the contour data within MATLAB, and outputs provided a localization of the crack path along specific x-y coordinates, represented schematically as the bi-linear line in Figure 5a, and linearly extending beyond the crack path termination defined by edge detection. This edge detection process, rather than manual visual identification, was used for crack path localization to allow for future automation of the methodology. Although the process did involve manual

manipulation in the current study, it is anticipated that more refinement of the edge detection process will allow for fully-automated fatigue crack characterization of DIC data without manual intervention. Once the initial crack path was identified through the edge detection process, data export paths orthogonal to the crack path were defined at discrete intervals along the crack path, shown as dashed lines in Figure 5a. Displacement values resulting from the DIC analyses were examined along each orthogonal path to determine the relative displacement occurring across the crack. Relative displacement for each orthogonal path was defined as the difference between plateau values on either side of the crack, shown in Figure 5b. Relative displacement extracted from the orthogonal paths was then plotted along the length of the crack path, creating figures similar to that in Figure 5c.

Each value of relative displacement along the crack path, Δ_i, was divided by the maximum relative displacement along the crack path, Δ_{max}, which typically occurs at the crack initiation site. This ratio was then subtracted from 100%, as presented in Equation 1, resulting in the convergence of relative displacement along the crack path, shown in Figure 5d. Convergence of relative displacement should theoretically approach 100% at the crack tip.

$$\text{Convergence} = 100\% - \frac{\Delta_i}{\Delta_{max}} \tag{1}$$

6.5 Discussion and Results of In-plane Testing

The described crack characterization methodology was applied for each load case within each crack length increment. Typical relative displacement and convergence plots for the specimen with a 25.4-mm (1.0-in.) long crack are shown in Figure 6 and Figure 7. The dotted vertical line indicates the crack length as measured through specimen compliance and verified optically.

Convergence values at known crack lengths were evaluated for each load case and are presented in Table 1 for the in-plane specimen trials. At crack lengths of 25.4, 38.1, and 50.8 mm (1.0, 1.5, and 2.0 in.), the majority of load cases resulted in convergence values over 90%, with many over 95%. Data for the 12.7-mm (0.5-in.) crack length did not converge as well, likely due to proximity to the machined notch and the resulting localized displacement behavior. As load range increased, calculated convergence values at the known crack length generally decreased, indicating that some relative displacement continued beyond the visibly-observable crack tip. It is well known that plasticity can influence behavior, with specimens exhibiting behavior corresponding to crack lengths longer than the physical crack size (Irwin 1960). Plasticity corrections are often used in linear-elastic fracture analyses (Anderson 1995), and iterative approximations commonly use a crack length increased by half of the plastic zone size (Collins et al. 2016). Therefore, the reduction in calculated convergence at higher values of stress intensity are likely to have been caused by crack tip plasticity. However, an investigation into the full quantification of any plasticity influence is beyond the scope of this paper.

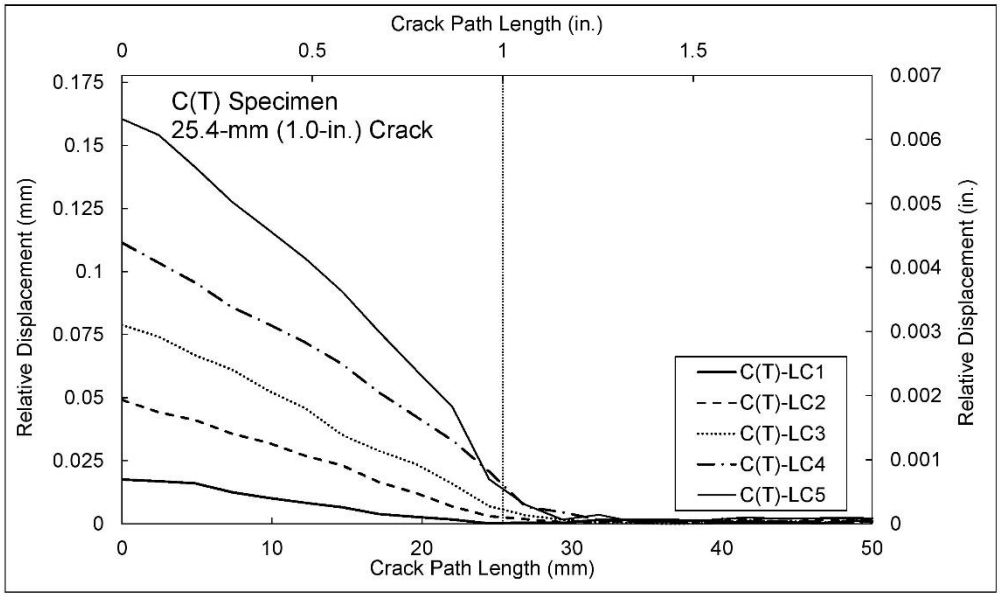

Figure 6. Relative displacement along the crack path for an in-plane specimen with a 25.4-mm (1.0-in) long crack.

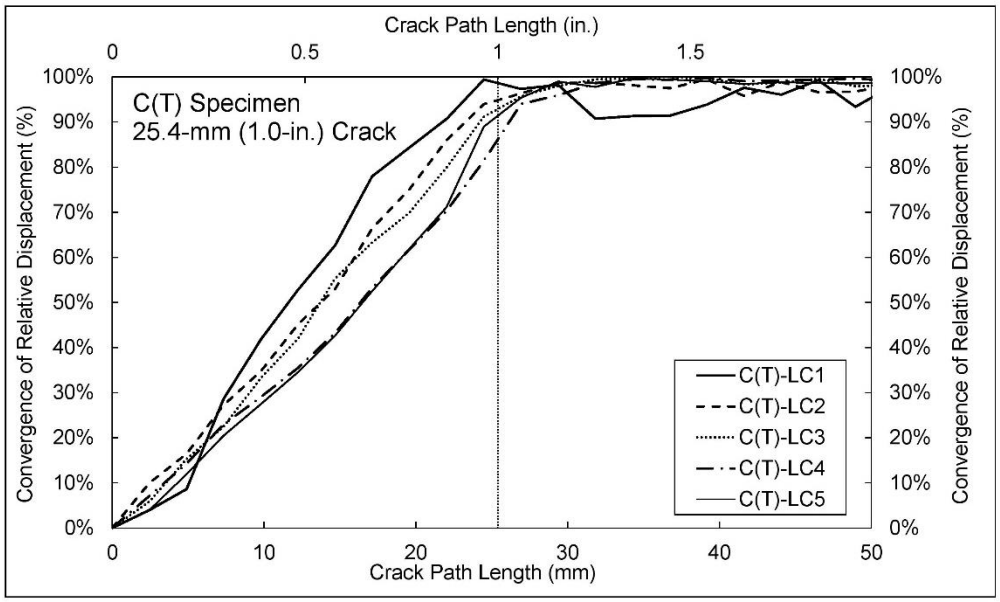

Figure 7. Convergence of relative displacement for an in-plane specimen with a 25.4-mm (1.0-in) long crack.

Chapter 7: Distortion-Induced Fatigue Crack

7.1 Out-of-Plane Test Specimen Description

The DIC inspection process and crack characterization methodology developed on the in-plane C(T) specimens was subsequently applied to a distortion-induced fatigue test setup for validation. An I-shaped plate girder subassembly was used as the test specimen, schematically presented in Figure 8a. Fabricated from A36 steel (ASTM 2019), the half-scale girder was 2845-mm (112-in.) long, 917-mm (36.1-in.) deep, and had a web thickness of 10 mm (0.375 in.). Attachments between cross-section elements were made with 5-mm (0.1875-in.) fillet welds. The girder subassembly was tested upside-down, such that the length of the bottom flange was connected rigidly to the laboratory floor, simulating the lateral stiffness provided by a concrete deck. A cross-frame was installed at mid-span of the girder, attached through a connection plate welded only to the girder web. The girder was loaded out-of-plane by applying a vertical load at the far end of the cross-frame, the direction of which is indicated in Figure 8a, producing a distortion-induced fatigue mechanism in the web-gap region between the flange and connection plate. Additional details characterizing the general distortion-induced fatigue test configuration can be found in Alemdar et al. (2014a).

Prior to collection of DIC measurements, the girder was loaded for 21,000 cycles at a load range of 2.2 kN to 25.5 kN (0.5 kip to 5.75 kip), resulting in the initiation and propagation of a fatigue crack in the web-gap region. The location of the crack is represented schematically in Figure 8b. As the location of the crack was known, the use of fluorescent dye penetrant allowed for a visual measurement of the fatigue crack located between the connection plate weld and the girder web. The total length of the observed distortion-induced fatigue crack was 44.5 mm (1.75

in.) and it consisted of three segments. Dimensions of each crack segment, reasonably idealized as linear and designated with letters in Figure 8b, were A = 9.7 mm (0.38 in.), B = 14.2 mm (0.56 in.), and C = 20.6 mm (0.81 in.).

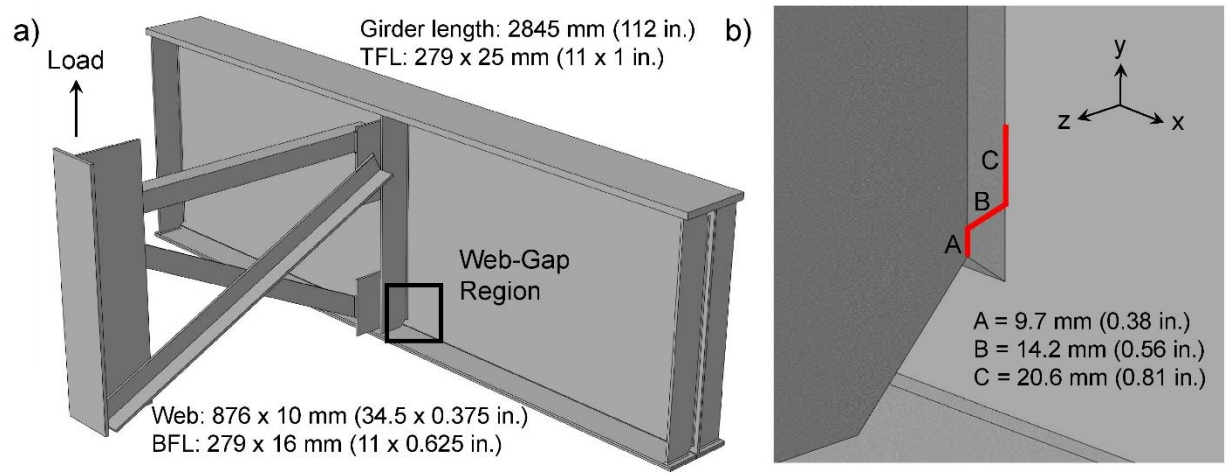

Figure 8. (a) Out-of-plane girder assembly; and (b) crack location and geometry.

7.2 Out-of-Plane Loading Protocol

Similar to the in-plane C(T) specimen tests, it was necessary to develop loading protocols representative of real steel bridge applications. Determination of appropriate load levels for the distortion-induced fatigue test was accomplished through the use of a finite element bridge model that was based on the full-scale proportions of the test setup. The modeled structure was a two-span continuous, non-skewed built-up steel bridge with four girder lines and a concrete deck. Linear-elastic material models were used for both the steel and deck elements, and the model contained approximately 4 million elements with 27 million degrees of freedom. Analytical models were based on those developed and validated as part of a previous study, additional details of which can be found in Hassel et al. (2013). A load representative of the AASHTO fatigue truck (AASHTO 2014) was applied in the finite element model, so that realistic levels of differential

vertical deflections between adjacent girders could be examined. From the finite element model, a representative value of differential girder deflection in the full-scale bridge system was found to be 2.5 mm (0.1 in.). Scaling down for the half-scale specimen resulted in a realistic target deflection of 1.3 mm (0.05 in.), which corresponded to an applied actuator load of 6.6 kN (1.5 kips) in the physical test setup. Seven load cases, DIF-LC1 through DIF-LC7, were then defined, applying load both above and below this value, as presented in Table 3 and schematically represented in Figure 9. The minimum applied load for all cases was 0.89 kN (0.2 kips), simulating the presence of dead load.

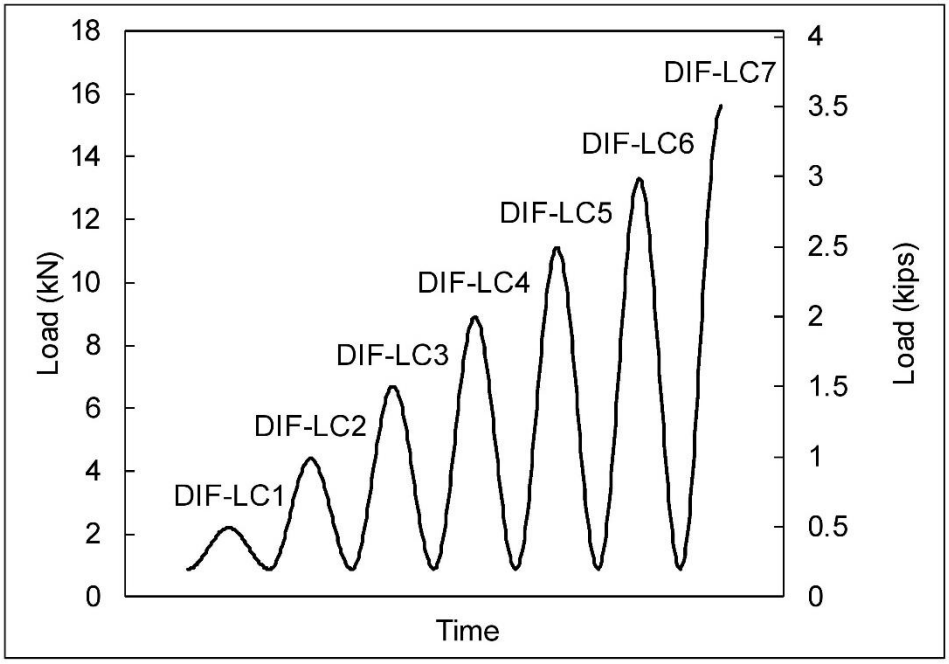

Figure 9. Schematic distortion-induced fatigue loading protocol.

Table 3. Distortion-induce fatigue crack length characterization

Load Case	Load Range kN (kips)	90% Convergence		95% Convergence	
		Computed Crack Length, mm (in.)	Error, %	Computed Crack Length, mm (in.)	Error, %
DIF-LC1	0.89-2.2 (0.2-0.5)	N/A	N/A	N/A	N/A
DIF-LC2	0.89-4.4 (0.2-1.0)	41.2 (1.62)	-7	46.1 (1.81)	4
DIF-LC3	0.89-6.7 (0.2-1.5)	39.7 (1.56)	-11	43.4 (1.71)	-2
DIF-LC4	0.89-8.9 (0.2-2.0)	44.4 (1.75)	0	50.6 (1.99)	14
DIF-LC5	0.89-11.1 (0.2-2.5)	36.7 (1.44)	-18	42.8 (1.69)	-4
DIF-LC6	0.89-13.3 (0.2-3.0)	38.9 (1.53)	-13	41.2 (1.62)	-7
DIF-LC7	0.89-15.6 (0.2-3.5)	42.8 (1.69)	-4	46.1 (1.81)	4
Average		40.6 (1.59)	-9	45.0 (1.77)	1

7.3 Out-of-Plane DIC Configuration

The configuration of the DIC setup for the distortion-induced fatigue tests was very similar to that used on the in-plane C(T) specimens, with a major difference being the use of a two-camera stereo setup. The distortion-induced fatigue specimen is shown in Figure 10a, with application of the high contrast surface pattern shown in Figure 10b. The web-gap region of the distortion-induced fatigue specimen was painted with a white background to allow for the application of a random, high contrast pattern. Spray paint was used to apply the black speckle pattern over the white background, with sizes ranging from 0.5 to 8.4 mm^2 (0.0007 to 0.013 $in.^2$), with the black pattern covering approximately one-third of the white-painted area. Manufacturer-provided calibration plates were used to calibrate the DIC system prior to the start of testing. The DIC hardware setup is shown in Figure 10c and Figure 10d, with the two cameras attached to vertical mounting bars connected to the tripod. The two cameras were separated by approximately 200 mm (8 in.) at a stereo angle of 31 degrees. As two cameras were used for the out-of-plane tests, VIC-

3D was used to analyze the data, and processing subset and step size were the same as that used for the in-plane analyses. Post-processing of the DIC data for coordinate transformation resulted in the x-axis located along the web-to-flange weld, the y-axis located along the stiffener-to-web weld, and the z-axis aligned with the direction of the cross-frame, as indicated in Figure 8b.

Figure 10. (a) Distortion-induced fatigue test frame; (b) applied high-contrast surface pattern in the web-gap region; (c) DIC hardware placement; and (d) detailed orientation of DIC hardware seen from above.

7.4 Application of Crack Characterization Methodology

The methodology initially developed for the case in which DIC was applied to the in-plane specimens was applied here to all load cases for the distortion-induced fatigue specimen. Z-axis displacement contour measurements were imported into the edge-detecting crack path algorithm. Although geometrically more complex than the crack on the C(T) specimen, the crack path obtained from the edge detection algorithm agreed with results from visual inspection. Typical visualized results obtained by DIC for the distortion-induced fatigue specimen are presented in Figure 11 in terms of maximum principal strain and displacement corresponding to the z-axis. Note that the horizontal discontinuities observable in Figure 11 are strain gage wires attached to the girder web during testing. Similar to the in-plane test results, strain-based DIC results allowed for a qualitative understanding of crack behavior, but were found to be of limited usefulness in the context of crack localization. Therefore, displacement data alone were used in the developed methodology. Relative displacements orthogonal to each segment of the crack tip were computed, extending beyond the crack tip perceived by the edge detection algorithm, and convergence values were calculated.

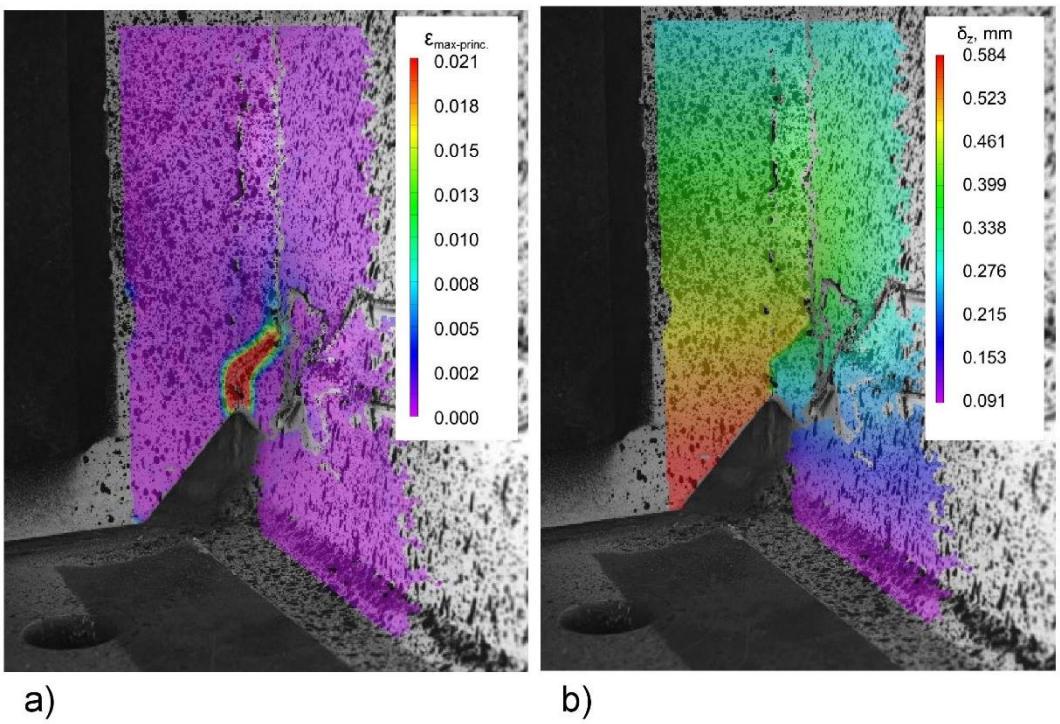

Figure 11. Typical visualized DIC results of the distortion-induced fatigue specimen in terms of: (a) maximum principal strain; and (b) *z*-direction displacement.

7.5 Discussion and Results of Distortion-Induced Fatigue Testing

Relative displacement along the crack path for each load case is shown in Figure 12, and convergence values for load cases DIF-LC2 through DIF-LC7 are presented in Figure 13. Relative displacements measured during DIF-LC1 were very small along the entire crack path length, resulting in high variability in convergence. This finding indicated that the methodology is not effective at this low load level, and established a threshold of applicability. Convergence values for DIF-LC1 are not presented in Figure 13.

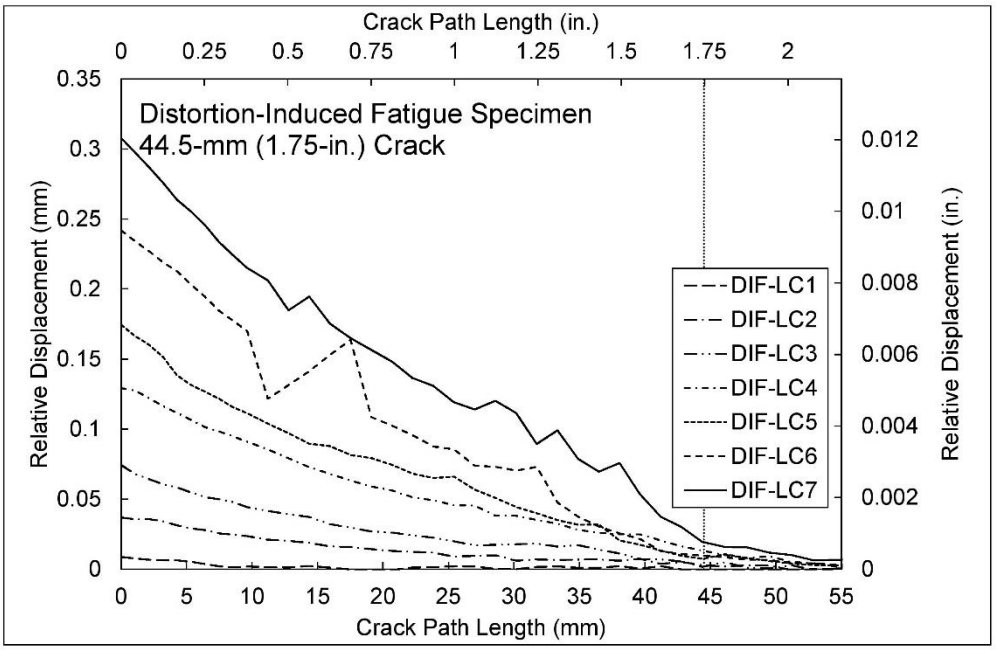

Figure 12. Relative displacement along the crack path length for the distortion-induced fatigue specimen.

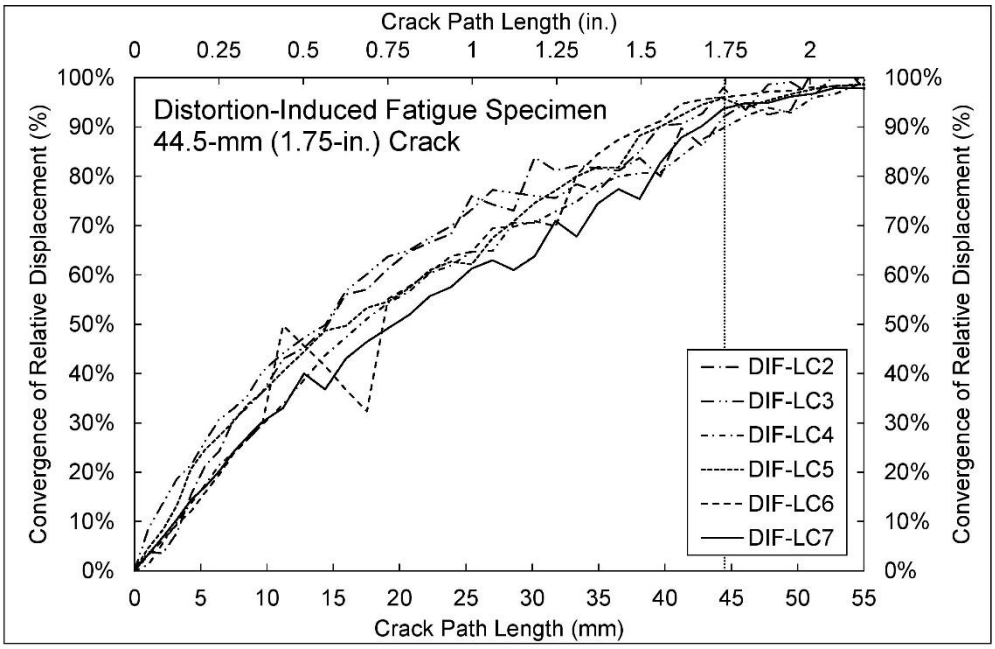

Figure 13. Convergence of relative displacement for the distortion-induced fatigue specimen.

Based on results from tests of the in-plane C(T) specimen, convergence thresholds of 90% and 95% were examined for the distortion-induced fatigue specimen. Table 3 presents results for these cases of 90% and 95% convergence compared with the optically-measured crack length of 44.5 mm (1.75 in.). Generally, using the 90% convergence threshold under-predicted crack length while using 95% convergence over-predicted crack length. The average crack length value corresponding to 90% convergence was 40.6 mm (1.59 in.), a 9% under-prediction. Evaluation of 95% convergence resulted in an average crack length of 45.0 mm (1.77 in.), only 1% greater than the optically-measured length. Although calculated convergence at known crack lengths in the C(T) specimens generally decreased, this was not the case for the distortion-induced fatigue specimen. This is seen in Table 3, where there is no clear trend in computed crack length error for the different load cases. Plastic zone size and shape are dependent on loading mode, and the mixed-mode loading of distortion-induced fatigue did not result in the same behavior as that observed for the in-plane C(T) specimens.

Chapter 8: Comparison of In-plane and Distortion-Induced Results

To facilitate a comparison between results from the DIC crack detection methodology applied to in-plane C(T) specimen and those from the out-of-plane fatigue specimen, applied stress intensity values were calculated for the distortion-induced load cases. Finite element analyses (Alemdar et al. 2014b) were used to determine Modes I, II, and III stress intensities at the crack tip for each load case, and an equivalent applied Mode I stress intensity was calculated. Modeling and data extraction techniques were validated based on known closed-form solutions of stress intensity for traditional fracture mechanics specimens (ASTM 2018). Applied stress intensity ranges for in-plane testing varied from 11 to 55 MPa√m (10 to 50 ksi√in) and values for distortion-induced fatigue testing were found to be between 10.1 and 40.5 MPa√m (9.2 and 36.9 ksi√in), providing adequate overlap to make a meaningful comparison.

Computed crack lengths were divided by the known crack lengths and plotted against applied stress intensity. This was done for each of the four in-plane crack lengths and for the distortion-induced fatigue crack. Evaluations of predicted crack length are presented for values of 90% and 95% convergence in Figure 14. Results of in-plane C(T) specimens are represented by the open symbols, while the distortion-induced fatigue results are represented by the filled symbols. All data points are connected with dashed lines to enhance clarity, and a solid horizontal line at 100% indicates an exact crack prediction. Data falling below the horizontal line signifies a prediction short of the physical crack length, while data above the line indicates a predicted crack length longer than the actual crack size.

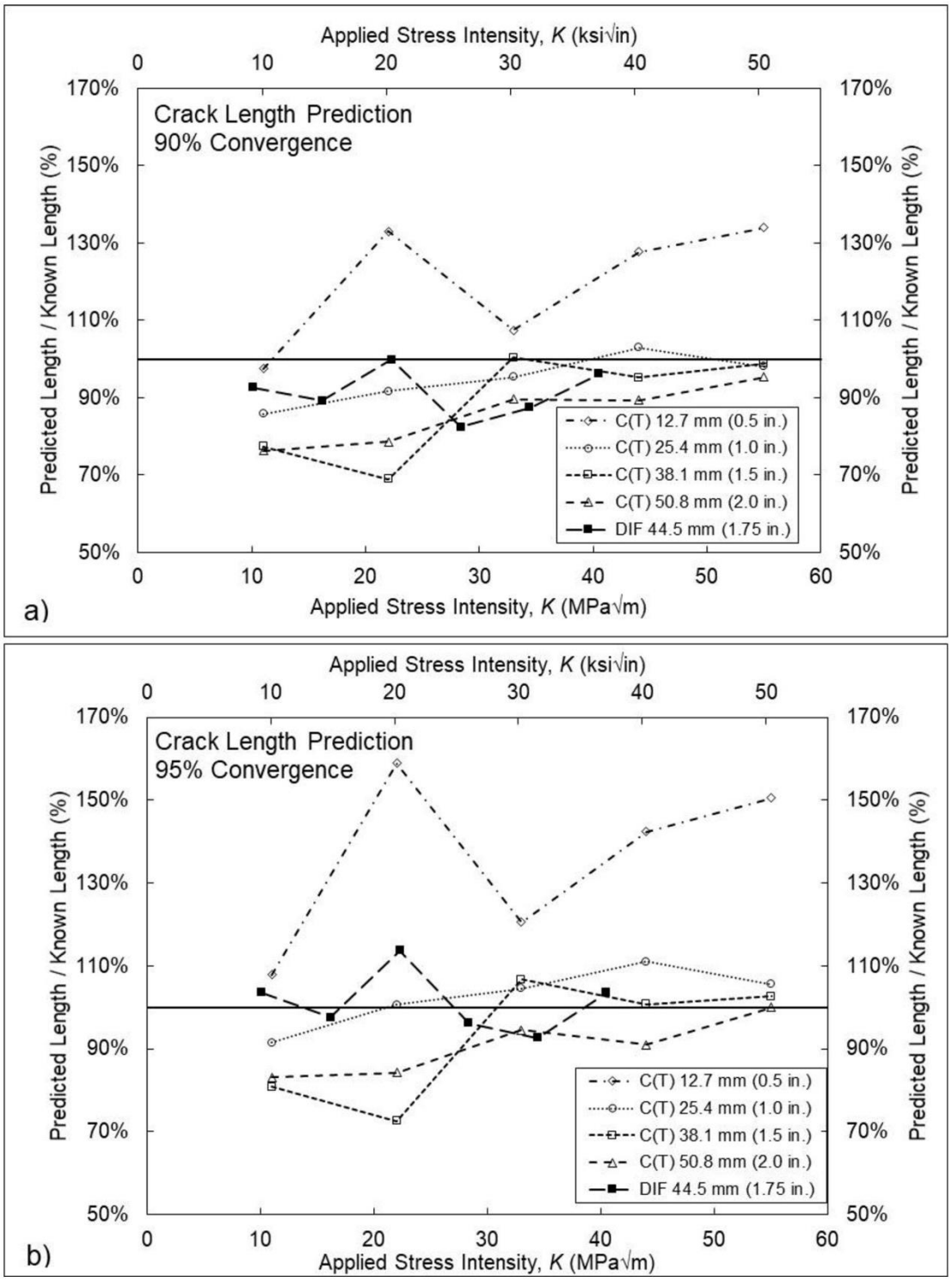

Figure 14. Crack length prediction at (a) 90%; and (b) 95% convergence.

Crack length predictions at both 90% and 95% convergence for the in-plane C(T) specimen with a 12.7-mm (0.5-in.) crack resulted in crack lengths longer than the physical crack size. For the majority of the in-plane specimens, however, 90% convergence resulted in crack lengths shorter than the physical crack size. The distortion-induced fatigue results were consistent with this behavior, with all predicted crack lengths shorter than the physical crack size. Predicted crack results at 95% convergence did not exhibit a consistent trend. Disregarding the 12.7-mm (0.5-in.) specimen, half of the in-plane results over-predicted crack length at 95% convergence, while the other half under-predicted crack length. Similar behavior was observed in the results of the out-of-plane distortion-induced fatigue specimen, with half of the load cases over-predicting and half under-predicting. In general, application of the crack characterization methodology to a distortion-induced fatigue specimen resulted in results similar to those for the case in which the methodology was applied to the in-plane specimens, indicating that the method developed is robust enough to be applied meaningfully to realistic fatigue applications.

Chapter 9: Conclusions and Future Work

This study presented the development of a methodology for using digital image correlation data as a crack detection and characterization tool. The methodology was initially developed in the context of in-plane fatigue testing C(T) specimens, and was then applied to a distortion-induced fatigue test specimen. Edge detection algorithms were applied to DIC displacement data contours to determine the crack path, and relative displacements orthogonal to the crack path were used to calculate a value of convergence, used to identify the crack tip. A theoretical convergence value of 100% should indicate the crack tip, where no relative displacement is occurring orthogonal to the crack path. However, results of in-plane testing indicated convergence between 90% and 95% corresponding to the actual crack length. Both the 90% and 95% convergence thresholds were investigated for the distortion-induced fatigue crack. For the load cases examined, 90% convergence resulted in a -9% error in crack length prediction, while 95% convergence produced an average crack length prediction only 1% beyond the known crack length. The threshold of applicability with respect to load was identified on the distortion-induced fatigue specimen, as the lowest load case examined was unable to produce adequate results. However, this threshold was found to be below fatigue loads expected on steel highway bridges, indicating the developed methodology has the potential for future bridge inspection application in the field.

Refinements to the methodology, continued examination of the impact of in-service conditions, and further development of fully automated algorithms and protocols are necessary prior to implementation of this methodology as a fatigue crack inspection tool. Further work in determining limits of the developed methodology should be undertaken, including the physical limits of DIC to produce data that can be analyzed. This should include variations in surface condition, lighting, and camera focus. As used in this study, DIC requires a precise setup and

operator interaction to provide the resolution presented. Further work is needed to develop a deployment mechanism capable of collecting DIC data with limited physical interaction, allowing for a potentially non-contact, automated inspection process. Additionally, the ability of 2D DIC utilizing a single camera setup to collect data on distortion-induced fatigue cracks should be examined. Investigating additional crack lengths and complex crack geometries, such as bifurcated distortion-induced fatigue cracks, would provide further insight into the potential strengths and weaknesses of the methodology. As used in this study, DIC requires extensive setup and operator interaction to provide the resolution presented.

Although previous research has examined the applicability of DIC analyses to fatigue crack identification and characterization, the vast majority has focused on in-plane loading. Additionally, most previous analyses resulted in qualitative measures of fatigue cracks. The work presented here represents a significant advancement in this area, with quantitative crack characterization applied to out-of-plane distortion-induced fatigue cracks. Advances are necessary to develop a fully automated methodology for detecting cracks on in-service steel highway bridges. The ability to quantify and characterize distortion-induced fatigue cracks with the use of DIC data demonstrates potential for the developed methodology to be fully automated in the future, improving the practice of fatigue inspection on steel bridges.

References

AASHTO. (2014). *LRFD bridge design specifications.* 7th ed. Washington, DC: AASHTO.

Alemdar, F., Nagati, D., Matamoros, A., Bennett, C., and Rolfe, S. (2014a). "Repairing Distortion-Induced Fatigue Cracks in Steel Bridge Girders Using Angles-with-Plate Retrofit Technique. I: Physical Simulations." *J. Struct. Eng.*, 10.1061/(ASCE)ST.1943-541X.0000876, 04014003.

Alemdar, F., Overman, T., Matamoros, A., Bennett, C., and Rolfe, S. (2014b). "Repairing Distortion-Induced Fatigue Cracks in Steel Bridge Girders Using Angles-with-Plate Retrofit Technique. II: Computer Simulations." *J. Struct. Eng.*, 10.1061/(ASCE)ST.1943-541X.0000874.

Alipour, M., Washlesky, S. J., & Harris, D. K. (2019). Field Deployment and Laboratory Evaluation of 2D Digital Image Correlation for Deflection Sensing in Complex Environments. Journal of Bridge Engineering, 24(4), 04019010. https://doi.org/10.1061/(ASCE)BE.1943-5592.0001363

American Society of Civil Engineers (ASCE). (2017). 2017 Infrastructure Report Card – Bridges, https://www.infrastructurereportcard.org/wp-content/uploads/2017/01/Bridges-Final.pdf

Anderson, T. L. (1995). *Fracture mechanics- Fundamentals and applications*, 2nd Ed., CRC Press, Boca Raton, FL.

ASTM International. (2019). *Standard specification for carbon structural steel*. ASTM A36-19. West Conshohocken, PA.

ASTM International. (2018). *Standard test method for fracture toughness*. ASTM E1820-18. West Conshohocken, PA.

Carroll, J. D., Abuzaid, W., Lambros, J., & Sehitoglu, H. (2013). High resolution digital image correlation measurements of strain accumulation in fatigue crack growth. *International Journal of Fatigue*, 57, 140-150. doi:10.1016/j.ijfatigue.2012.06.010

Carroll, J., Efstathiou, C., Lambros, J., Sehitoglu, H., Hauber, B., Spottswood, S., & Chona, R. (2009). Investigation of fatigue crack closure using multiscale image correlation experiments. *Engineering Fracture Mechanics*, 76(15), 2384-2398. doi:10.1016/j.engfracmech.2009.08.002

Chen, F., Chen, X., Xie, X., Feng, X., & Yang, L. (2013). Full-field 3D measurement using multi-camera digital image correlation system. Optics and Lasers in Engineering,51(9), 1044-1052. doi:10.1016/j.optlaseng.2013.03.001

Cigada, A., Mazzoleni, P., & Zappa, E. (2014). Vibration monitoring of multiple bridge points by means of a unique vision-based measuring system. Experimental Mechanics, 54(2), 255-271.

Collins, W., Sherman, R., Leon, R., & Connor, R. (2016). "State-of-the-art fracture characterization. I: Master curve analysis of legacy bridge steels." *J. Bridge Eng.* 21 (12): 04016097. https://doi.org/10.1061/(ASCE)BE.1943-5592.0000954.

Dhanasekar, M., Prasad, P., Dorji, J., & Zahra, T. (2018). Serviceability Assessment of Masonry Arch Bridges Using Digital Image Correlation. Journal of Bridge Engineering, 24(2), 04018120. https://doi.org/10.1061/(ASCE)BE.1943-5592.0001341

Federal Highway Administration (FHWA). (2004). *National bridge inspection standards*, Federal Register, 69 (239)

Fisher, J. W. (1984). *Fatigue and fracture in steel bridges. Case studies*. J. Wiley and Sons, Limited; Sussex, England.

Hamam, R., Hild, F., & Roux, S. (2007). Stress Intensity Factor Gauging by Digital Image Correlation: Application in Cyclic Fatigue. Strain, 43(3), 181-192. doi:10.1111/j.1475-1305.2007.00345.x

Hassel, H., Bennett, C., Matamoros, A., and Rolfe, S. (2013). "Parametric analysis of cross-frame layout on distortion-induced fatigue in skewed steel bridges." *J. Bridge Eng.*, (18)7, 601-611. doi:10.1061/(ASCE)BE.1943-5592.0000388.

Helfrick, M. N., Niezrecki, C., Avitabile, P., & Schmidt, T. (2011). 3D digital image correlation methods for full-field vibration measurement. Mechanical Systems and Signal Processing, 25(3), 917-927. doi:10.1016/j.ymssp.2010.08.013

Hutt, T., & Cawley, P. (2009). Feasibility of digital image correlation for detection of cracks at fastener holes. NDT & E International,42(2), 141-149. doi:10.1016/j.ndteint.2008.10.008

Irwin, G. R. (1960). "Plastic zone near a crack and fracture toughness." *7th Sagamore Ordnance Materials Research Conf.*, Ordnance Materials Research Office and the Office of Ordnance Research of the U.S. Army, Raquette Lake, NY, 63-78.

Lorenzino, P., Beretta, G., & Navarro, A. (2014). Application of digital image correlation (DIC) in resonance machines for measuring fatigue crack growth. Frattura Ed Integrita Strutturale,(30), 369-374. doi:dx.doi.org/10.3221/IGF-ESIS.30.44

Lee, J. J., & Shinozuka, M. (2006). A vision-based system for remote sensing of bridge displacement. NDT & E International, 39(5), 425-431. doi.org/10.1016/j.ndteint.2005.12.003

Nowell, D., Paynter, R. J., & Matos, P. F. (2010). Optical methods for measurement of fatigue crack closure: Moiré interferometry and digital image correlation. Fatigue & Fracture of Engineering Materials & Structures,33(12), 778-790. doi:10.1111/j.1460-2695.2010.01447.x

Pan, B., Tian, L., & Song, X. (2016). Real-time, non-contact and targetless measurement of vertical deflection of bridges using off-axis digital image correlation. Ndt & E International, 79, 73-80. https://doi.org/10.1016/j.ndteint.2015.12.006

Parker, J. R. (2011). *Algorithms for image processing and computer vision*. 2nd ed. Wiley, New York.

Ribeiro, D., Calçada, R., Ferreira, J., & Martins, T. (2014). Non-contact measurement of the dynamic displacement of railway bridges using an advanced video-based system. Engineering Structures, 75, 164-180. https://doi.org/10.1016/j.engstruct.2014.04.051

Rupil, J., Roux, S., Hild, F., & Vincent, L. (2011). Fatigue microcrack detection with digital image correlation. The Journal of Strain Analysis for Engineering Design,46(6), 492-509. doi:10.1177/0309324711402764

Sutton, M. A. (2007). Three-dimensional digital image correlation to quantify deformation and crack-opening displacement in ductile aluminum under mixed-mode I/III loading. *Optical Engineering*, 46(5), 051003. doi:10.1117/1.2741279

Vanlanduit, S., Vanherzeele, J., Longo, R., & Guillaume, P. (2009). A digital image correlation method for fatigue test experiments. Optics and Lasers in Engineering,47(3-4), 371-378. doi:10.1016/j.optlaseng.2008.03.016

Whitehead, J. (2015). “Probability of detection study for visual inspection of steel bridges.” Master’s Thesis, Purdue University, West Lafayette, IN.

Zhang, R., & He, L. (2012). Measurement of mixed-mode stress intensity factors using digital image correlation method. Optics and Lasers in Engineering, 50(7), 1001-1007. doi:10.1016/j.optlaseng.2012.01.009

Zhao, Y., & Roddis, W. M. K. (2004). Fatigue Prone Steel Bridge Details: Investigation and Recommended Repairs, *K-TRAN: KU-99-2, Final Report.* Kansas Department of Transportation, Topeka, KS.

Zhao Z, and Haldar A. (1996). Bridge fatigue damage evaluation and updating using non-destructive inspections. *Engineering fracture mechanics*. 53(5), 775-88

Appendix A: In-Plane Testing Data and Results

Shown below is a compilation of data for the in-plane test specimen. The plots and images are sorted by crack length. The data includes the following figures: relative displacement along the crack path, convergence of relative displacement, original image, and strain and displacement contours for each load case overlaid on top of the original image.

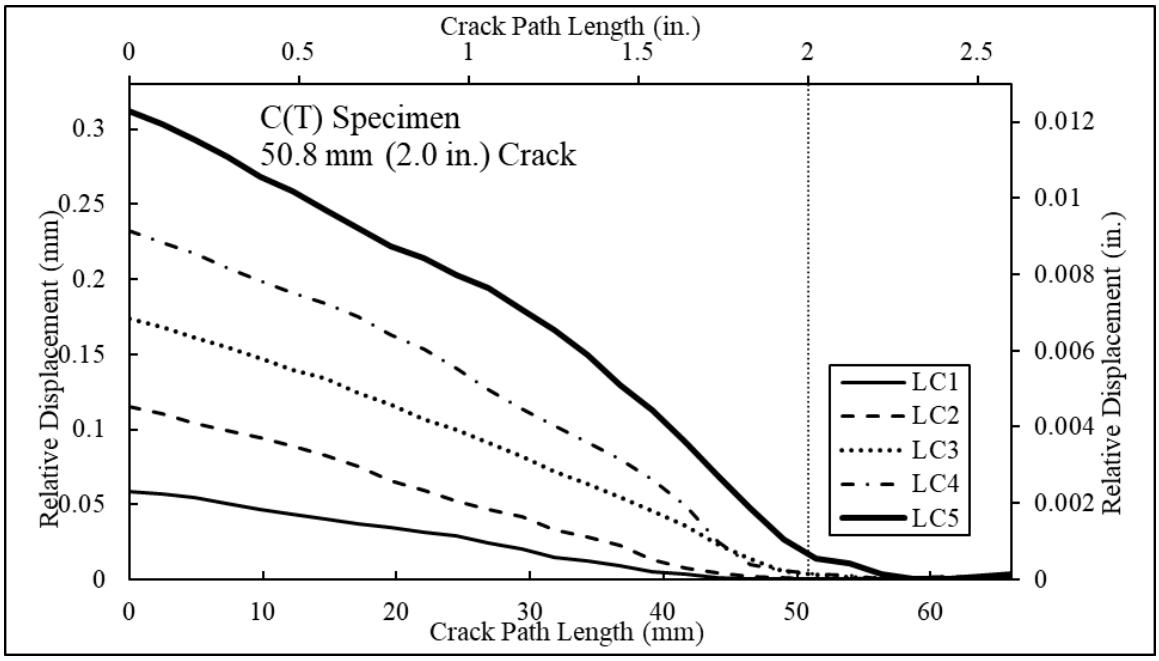

Figure A-1. Relative displacement along crack path for 50.8 mm (2.0 in.) cracked in-plane specimen.

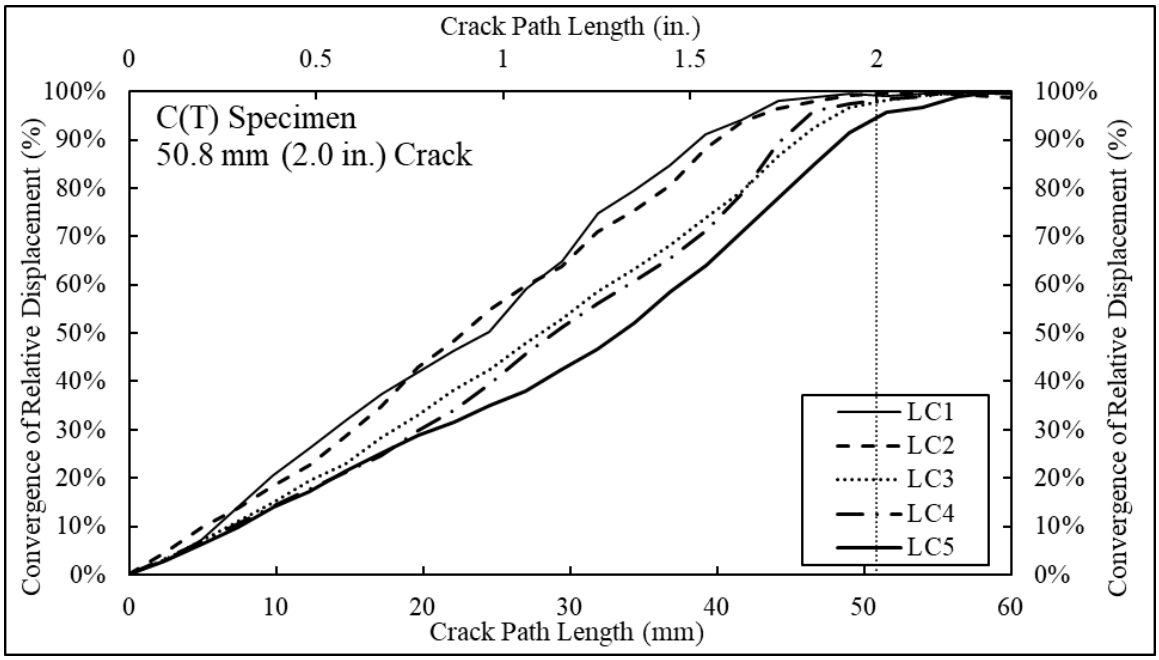

Figure A-2. Convergence of relative displacement for 50.8 mm (2.0 in.) cracked in-plane specimen.

Figure A-3. Unloaded C(T) specimen with 50.8 mm (2.0 in.) in-plane crack.

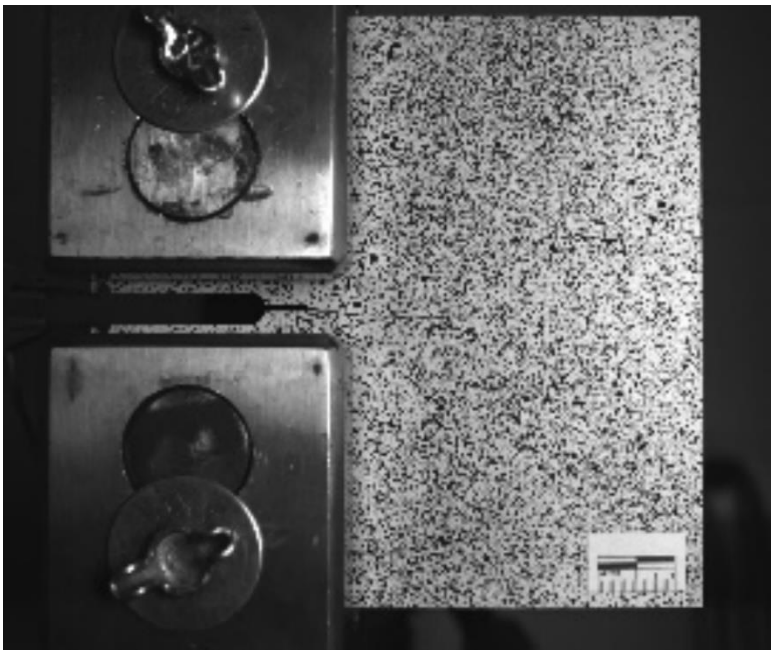

Figure A-4. C(T) specimen with 50.8 mm (2.0 in.) in-plane crack under loading case 1.

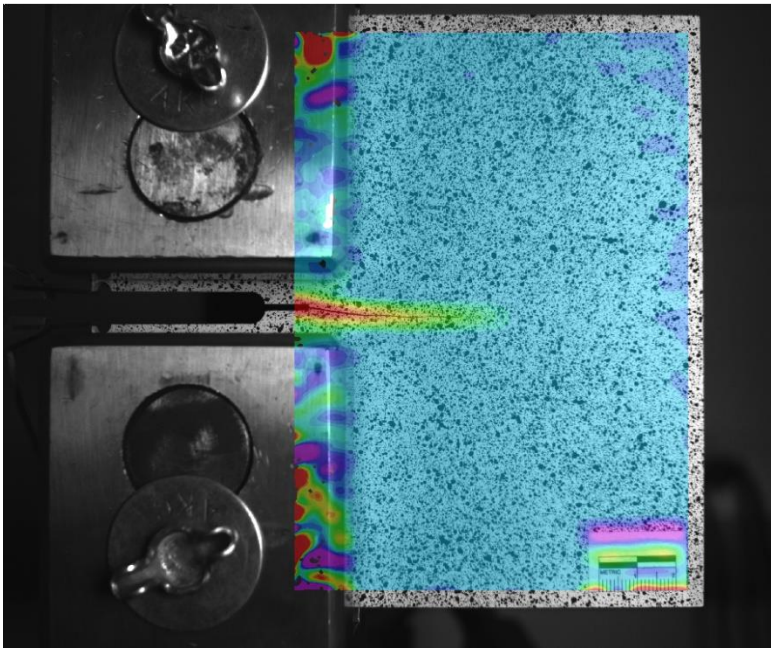

Figure A-5. Strain contours for C(T) specimen with 50.8 mm (2.0 in.) in-plane crack under loading case 1.

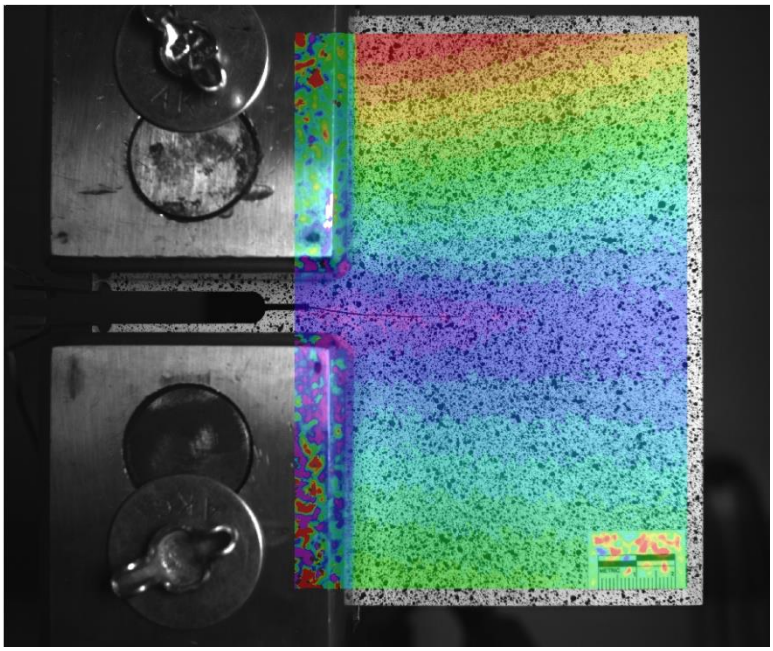

Figure A-6. Displacement contours for C(T) specimen with 50.8 mm (2.0 in.) in-plane crack under loading case 1.

Figure A-7. C(T) specimen with 50.8 mm (2.0 in.) in-plane crack under loading case 2.

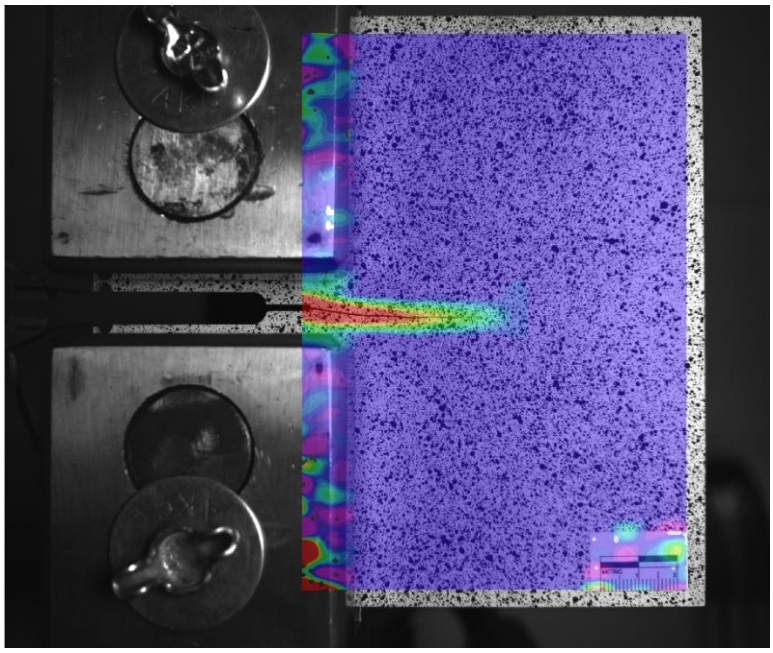

Figure A-8. Strain contours for C(T) specimen with 50.8 mm (2.0 in.) in-plane crack under loading case 2.

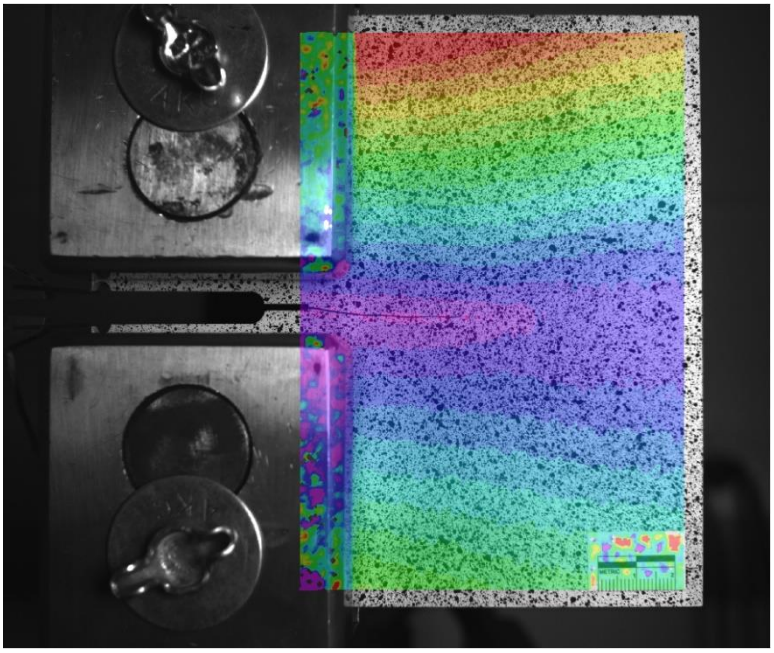

Figure A-9. Displacement contours for C(T) specimen with 50.8 mm (2.0 in.) in-plane crack under loading case 2.

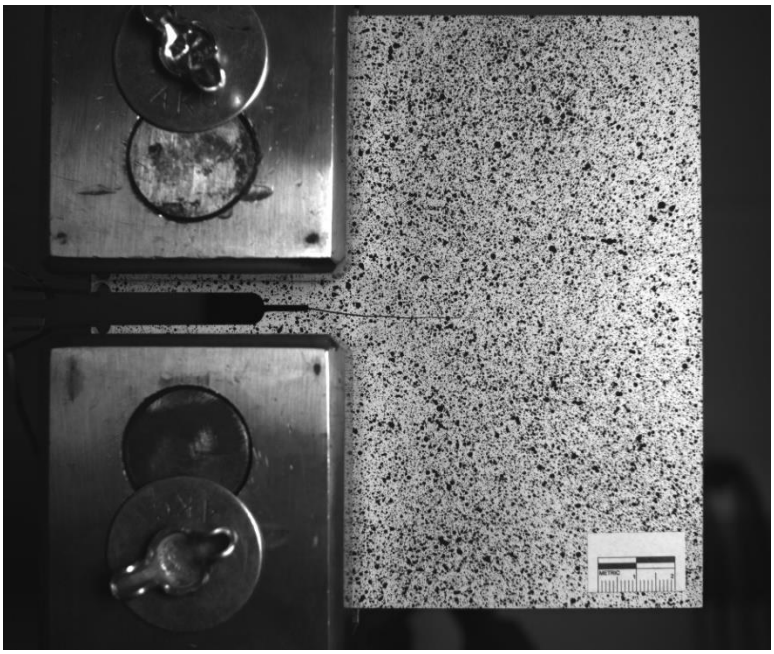

Figure A-10. C(T) specimen with 50.8 mm (2.0 in.) in-plane crack under loading case 3.

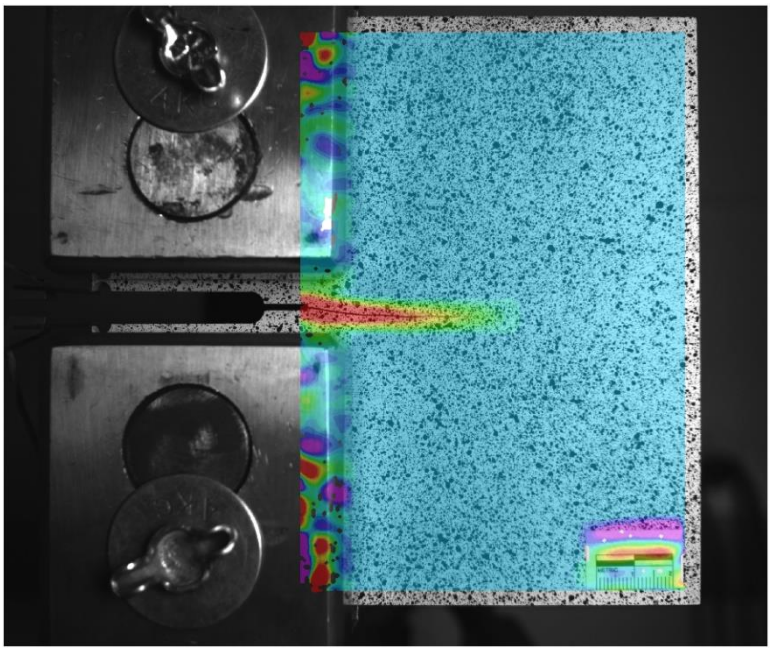

Figure A-11. Strain contours for C(T) specimen with 50.8 mm (2.0 in.) in-plane crack under loading case 3.

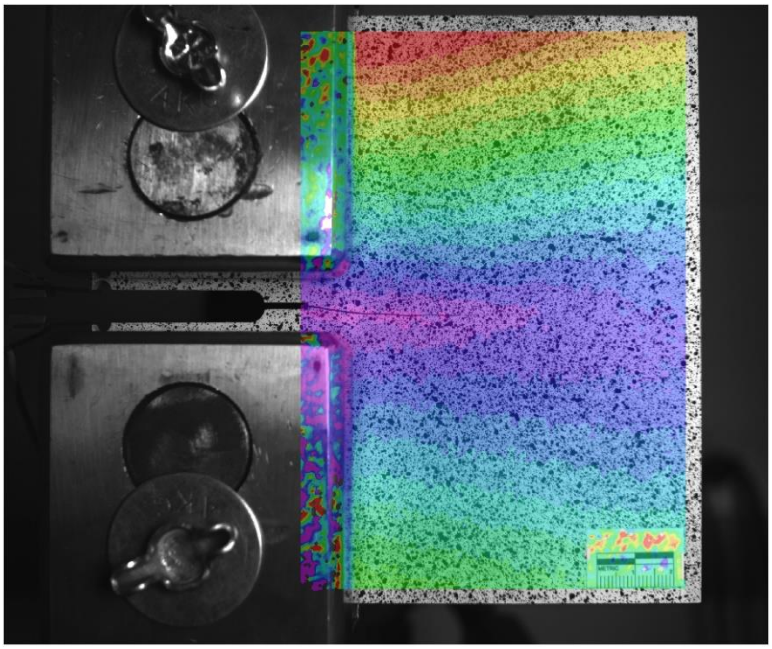

Figure A-12. Displacement contours for C(T) specimen with 50.8 mm (2.0 in.) in-plane crack under loading case 3.

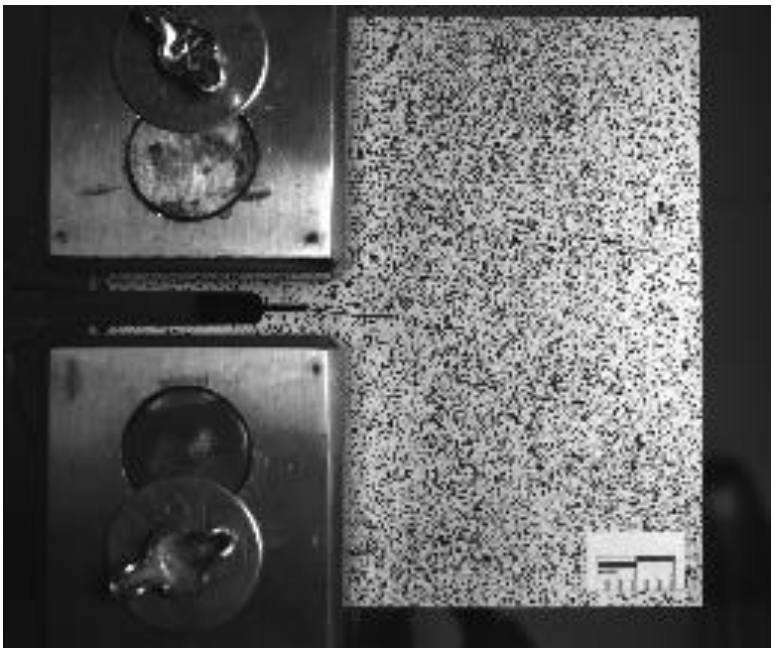

Figure A-13. C(T) specimen with 50.8 mm (2.0 in.) in-plane crack under loading case 4.

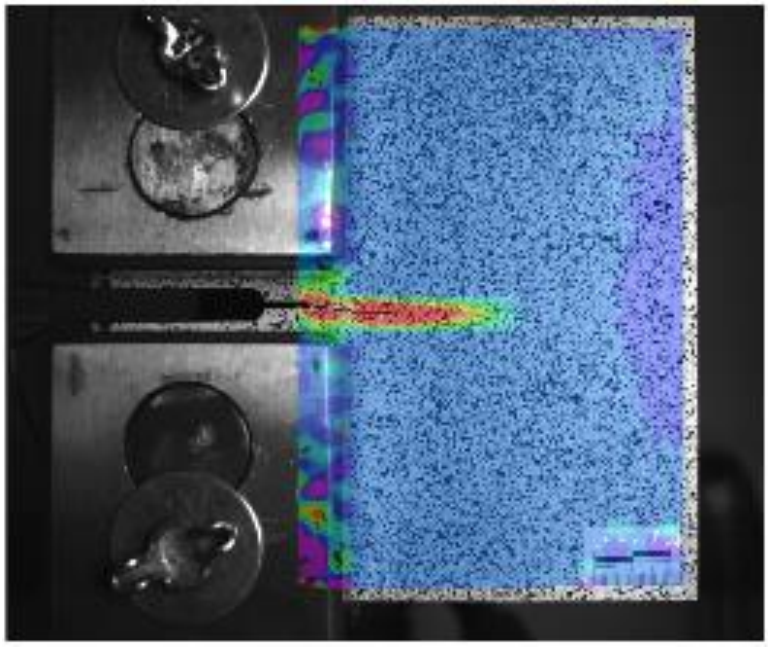

Figure A-14. Strain contours for C(T) specimen with 50.8 mm (2.0 in.) in-plane crack under loading case 4.

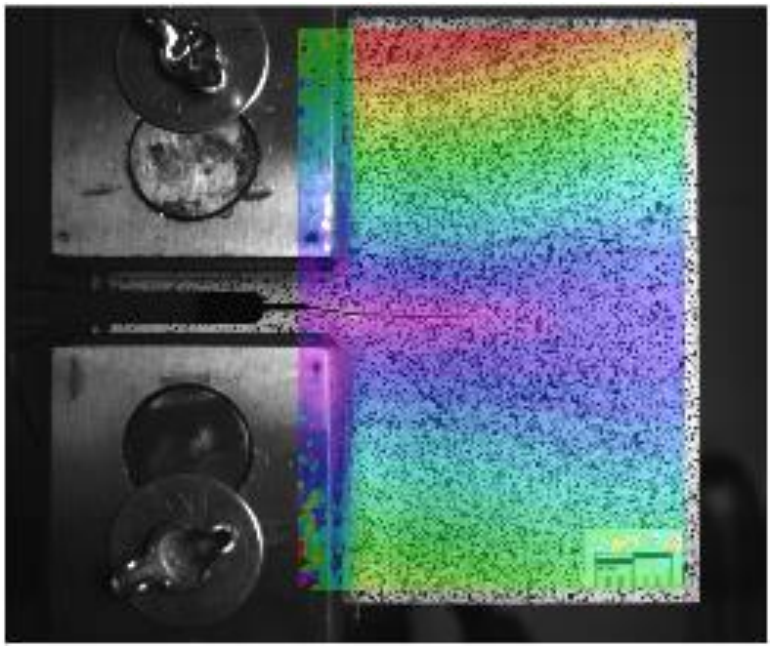

Figure A-15. Displacement contours for C(T) specimen with 50.8 mm (2.0 in.) in-plane crack under loading case 4.

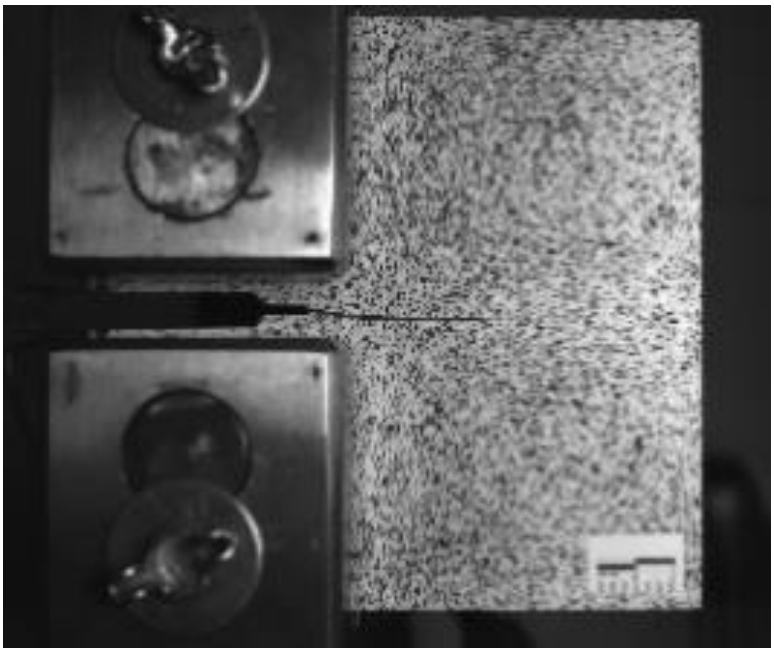

Figure A-16. C(T) specimen with 50.8 mm (2.0 in.) in-plane crack under loading case 5.

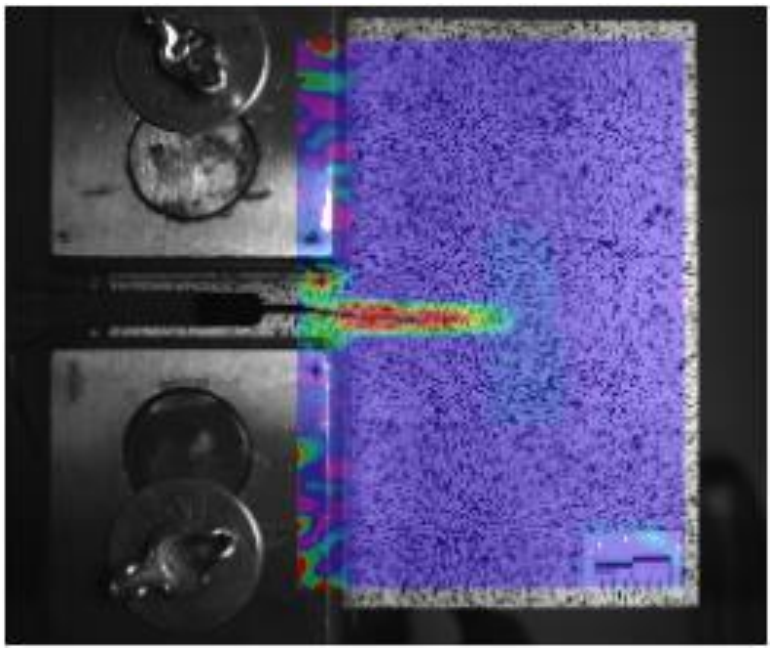

Figure A-17. Strain contours for C(T) specimen with 50.8 mm (2.0 in.) in-plane crack under loading case 5.

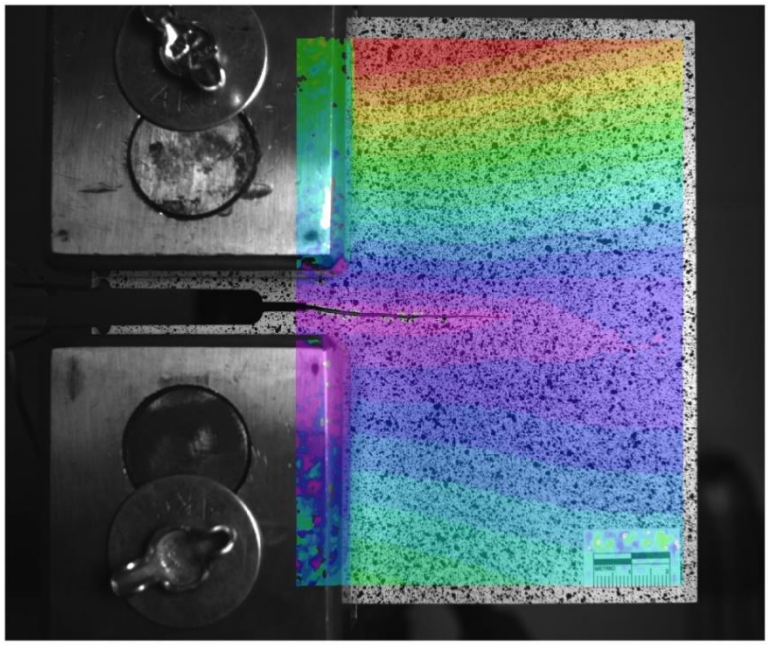

Figure A-18. Displacement contours for C(T) specimen with 50.8 mm (2.0 in.) in-plane crack under loading case 5.

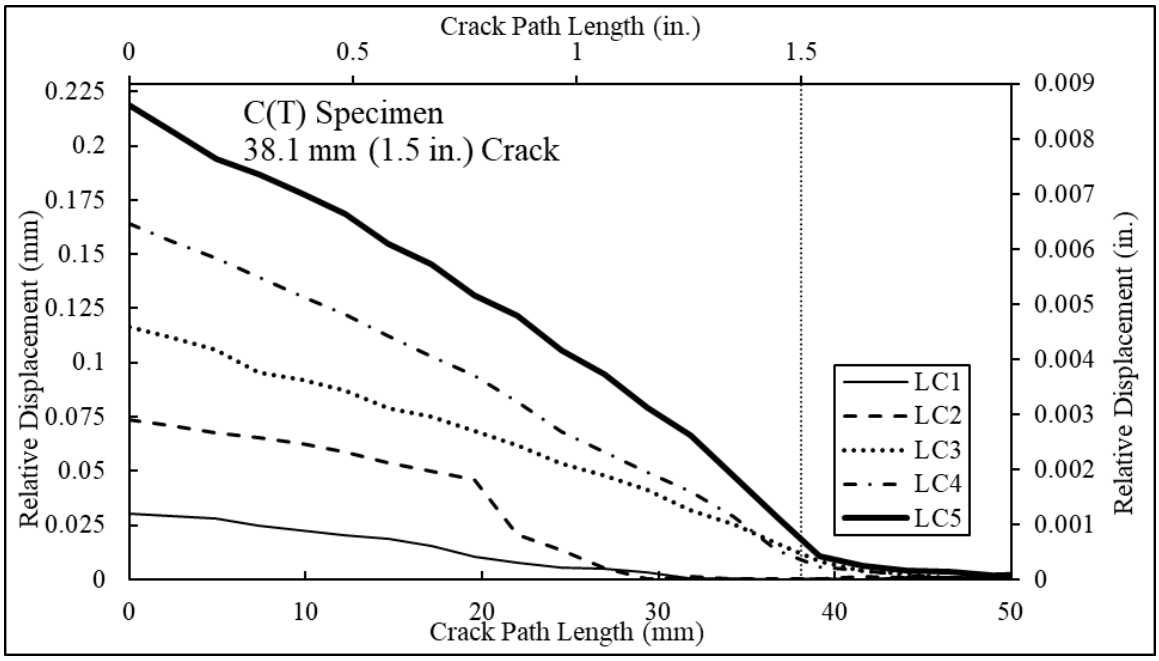

Figure A-19. Relative displacement along crack path for 38.1 mm (1.5 in.) cracked in-plane specimen.

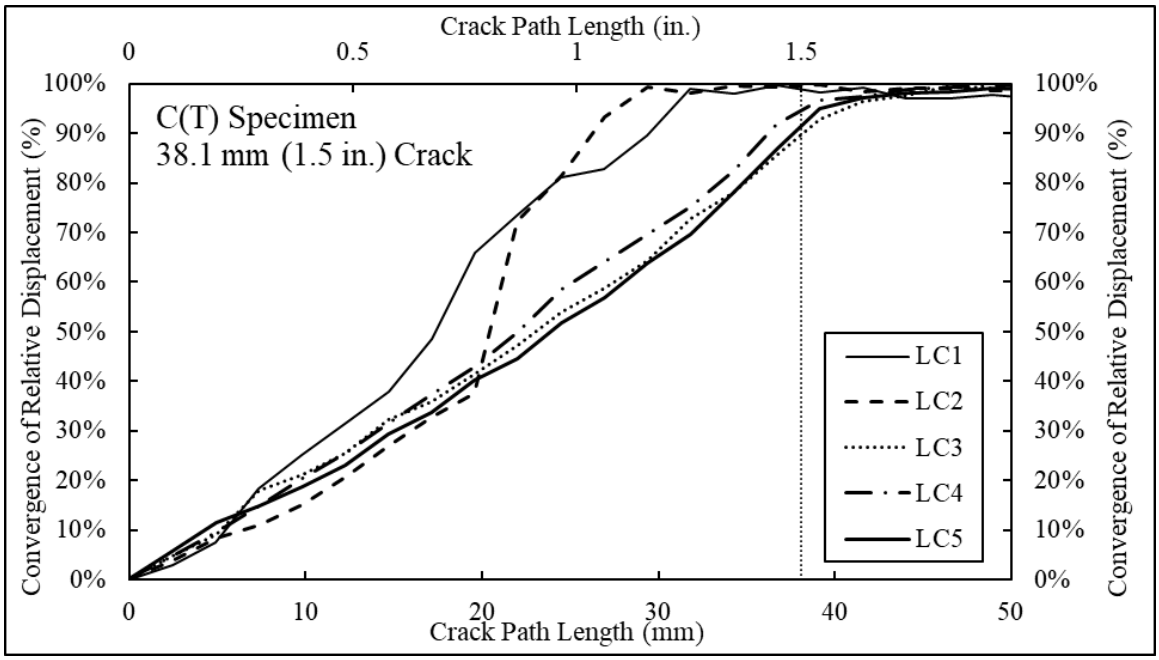

Figure A-20. Convergence of relative displacement for 38.1 mm (1.5 in.) cracked in-plane specimen.

Figure A-21. Unloaded C(T) specimen with 38.1 mm (1.5 in.) in-plane crack.

Figure A-22. C(T) specimen with 38.1 mm (1.5 in.) in-plane crack under loading case 1.

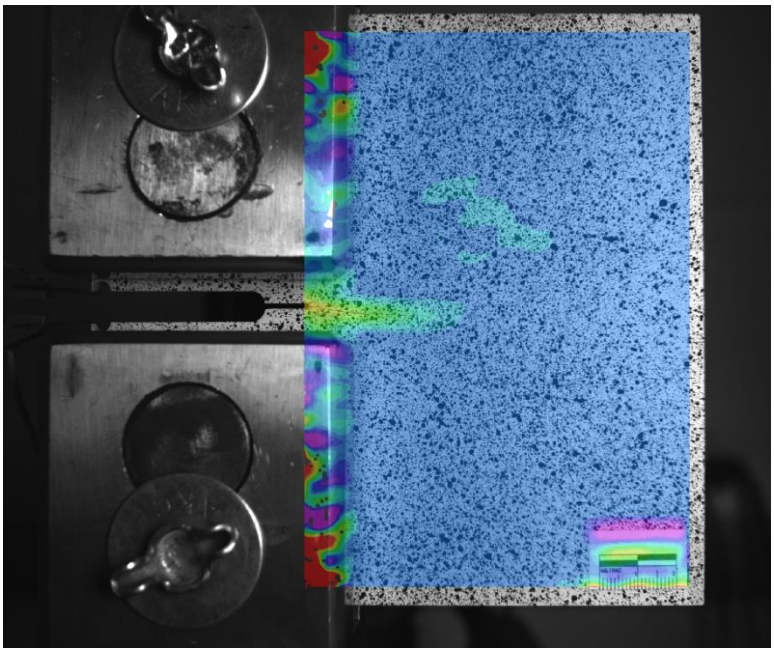

Figure A-23. Strain contours for C(T) specimen with 38.1 mm (1.5 in.) in-plane crack under loading case 1.

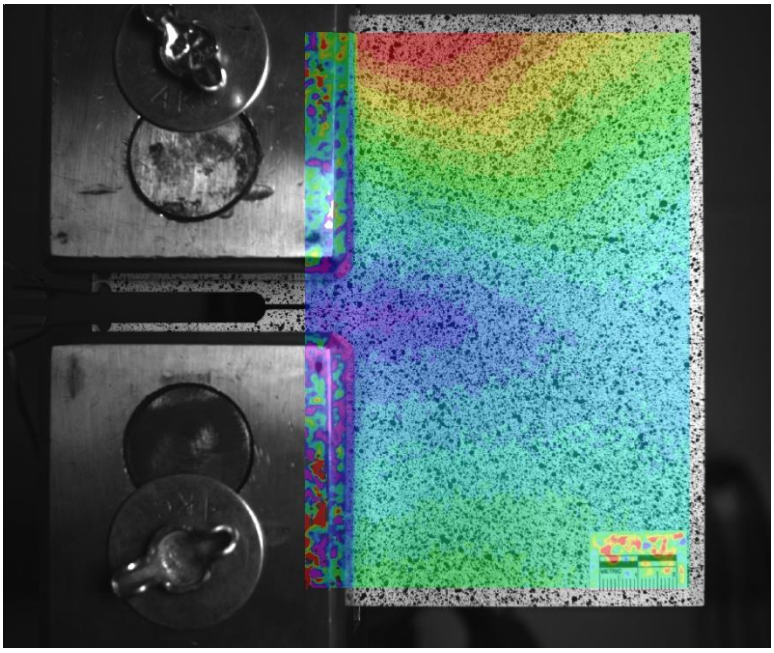

Figure A-24. Displacement contours for C(T) specimen with 38.1 mm (1.5 in.) in-plane crack under loading case 1.

Figure A-25. C(T) specimen with 38.1 mm (1.5 in.) in-plane crack under loading case 2.

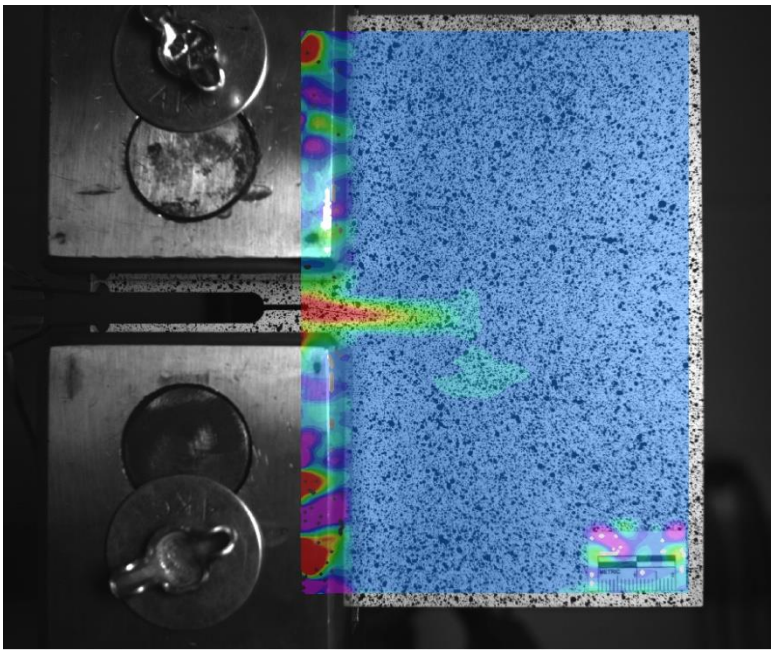

Figure A-26. Strain contours for C(T) specimen with 38.1 mm (1.5 in.) in-plane crack under loading case 2.

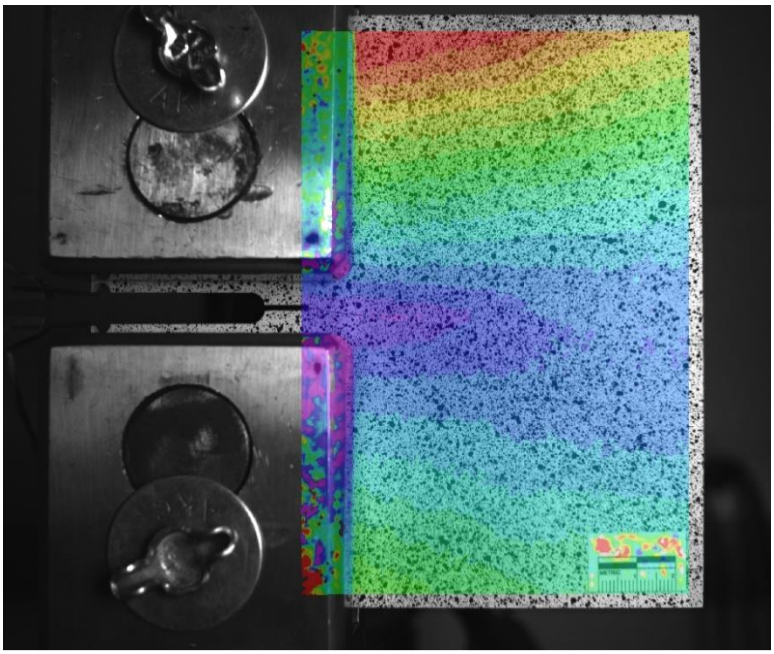

Figure A-27. Displacement contours for C(T) specimen with 38.1 mm (1.5 in.) in-plane crack under loading case 2.

Figure A-28. C(T) specimen with 38.1 mm (1.5 in.) in-plane crack under loading case 3.

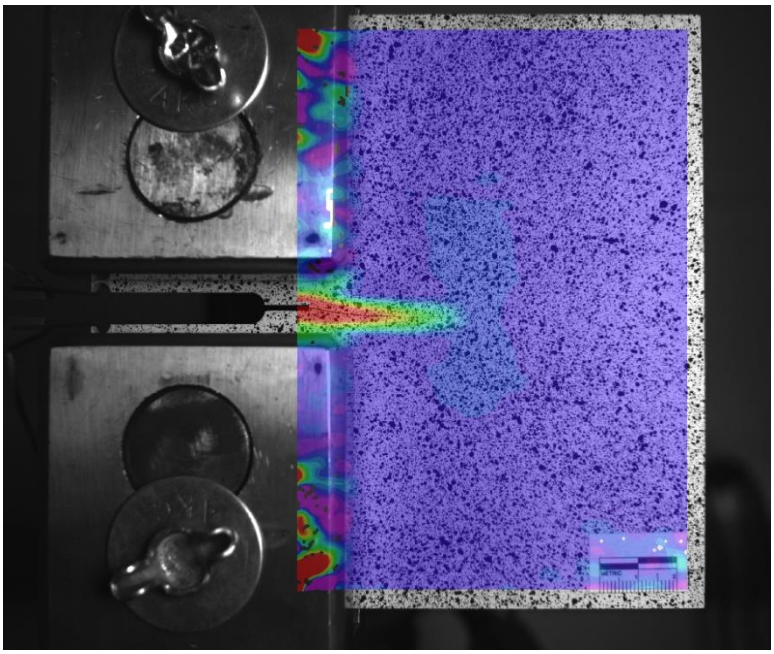

Figure A-29. Strain contours for C(T) specimen with 38.1 mm (1.5 in.) in-plane crack under loading case 3.

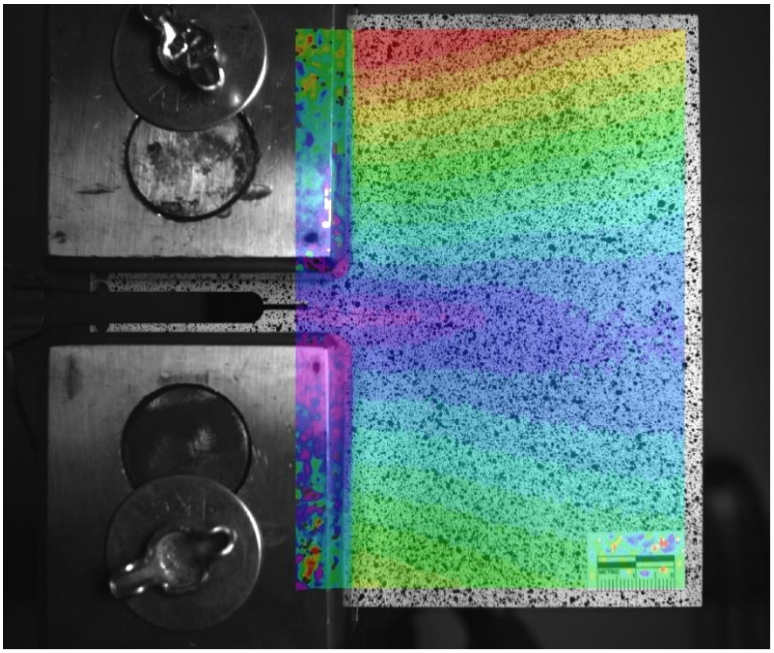

Figure A-30. Displacement contours for C(T) specimen with 38.1 mm (1.5 in.) in-plane crack under loading case 3.

Figure A-31. C(T) specimen with 38.1 mm (1.5 in.) in-plane crack under loading case 4.

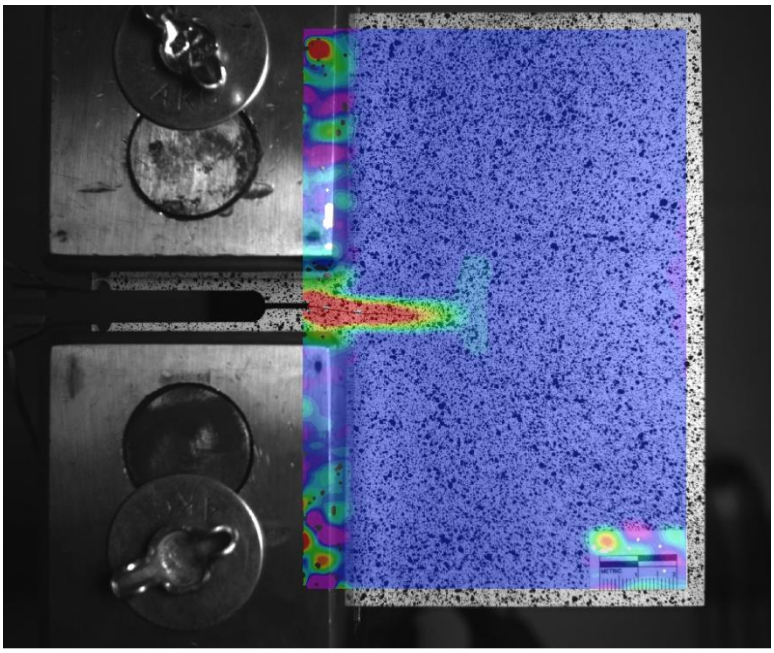

Figure A-32. Strain contours for C(T) specimen with 38.1 mm (1.5 in.) in-plane crack under loading case 4.

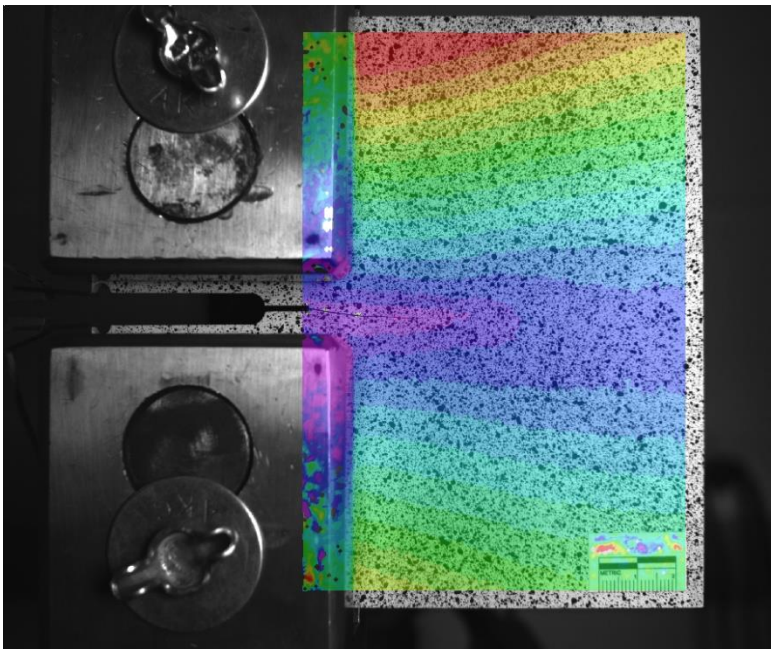

Figure A-33. Displacement contours for C(T) specimen with 38.1 mm (1.5 in.) in-plane crack under loading case 4.

Figure A-34. C(T) specimen with 38.1 mm (1.5 in.) in-plane crack under loading case 5.

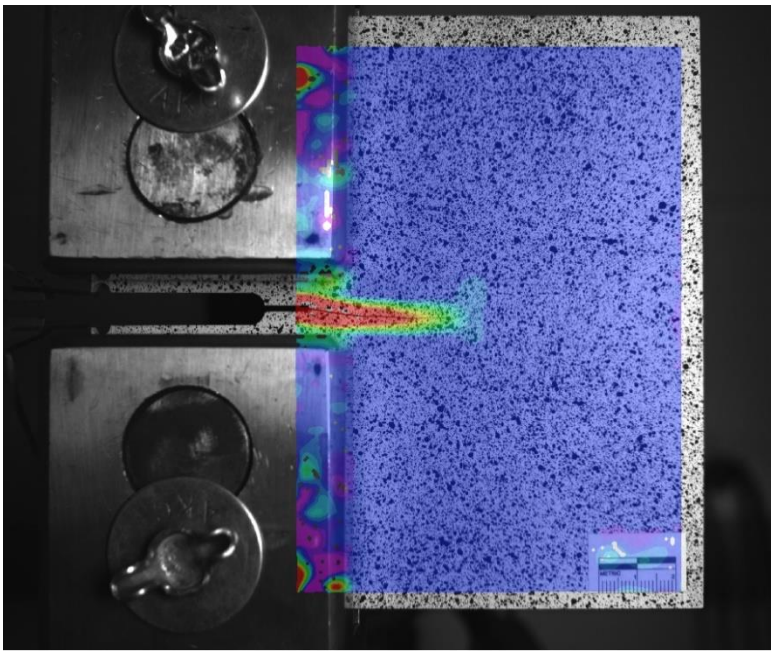

Figure A-35. Strain contours for C(T) specimen with 38.1 mm (1.5 in.) in-plane crack under loading case 5.

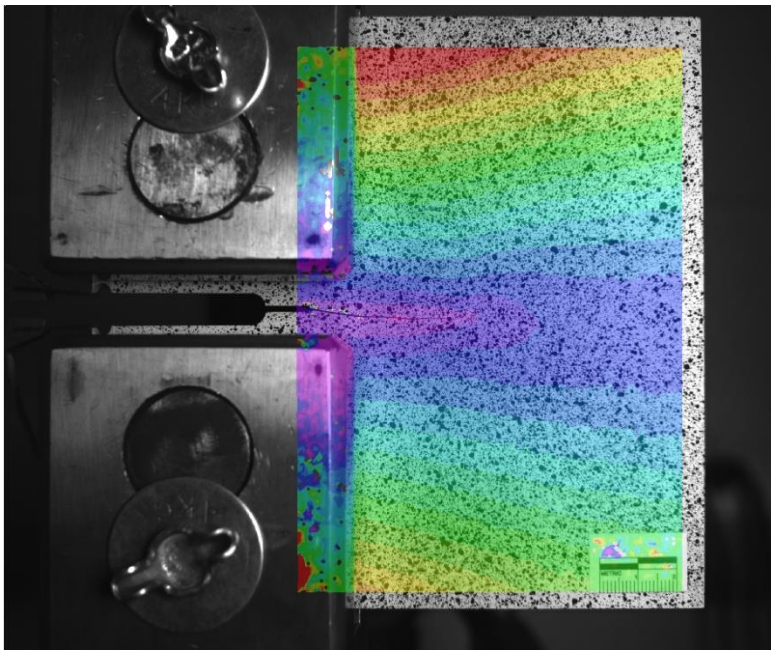

Figure A-36. Displacement contours for C(T) specimen with 38.1 mm (1.5 in.) in-plane crack under loading case 5.

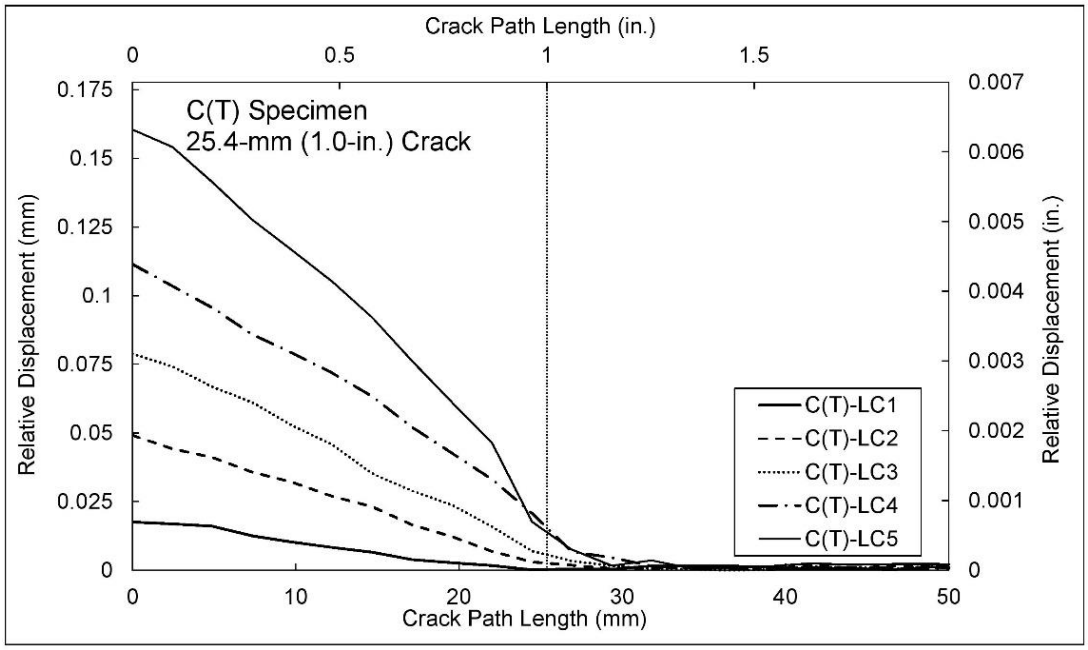

Figure A-37. Relative displacement along crack path for 25.4 mm (1.0 in.) cracked in-plane specimen.

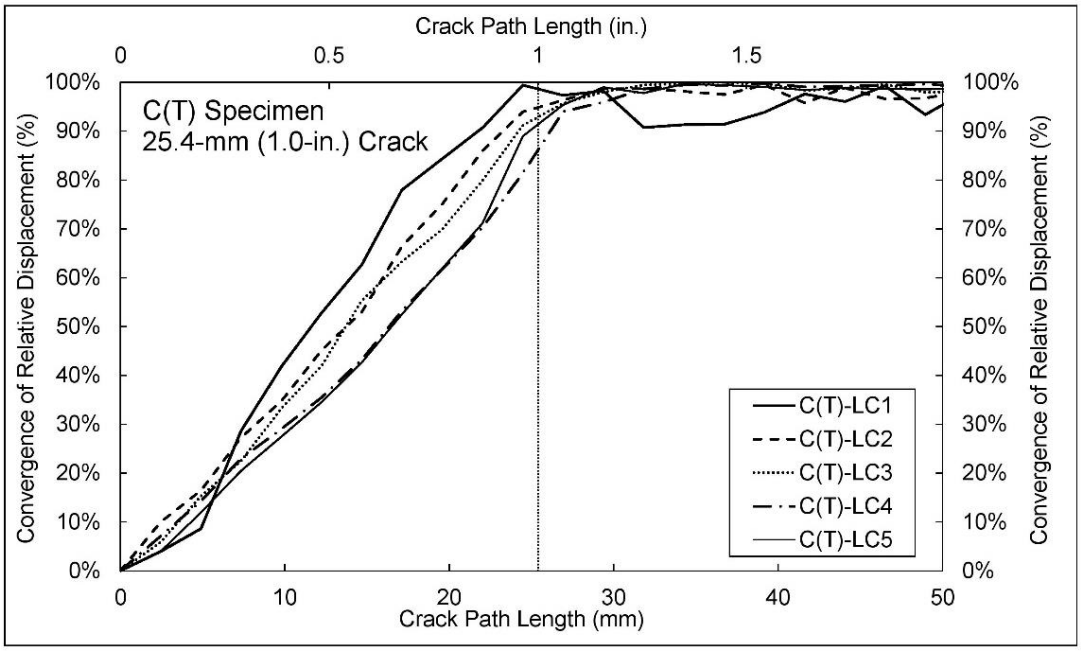

Figure A-38. Convergence of relative displacement for 25.4 mm (1.0 in.) cracked in-plane specimen.

Figure A-39. Unloaded C(T) specimen with 25.4 mm (1.0 in.) in-plane crack.

Figure A-40. C(T) specimen with 25.4 mm (1.0 in.) in-plane crack under loading case 1.

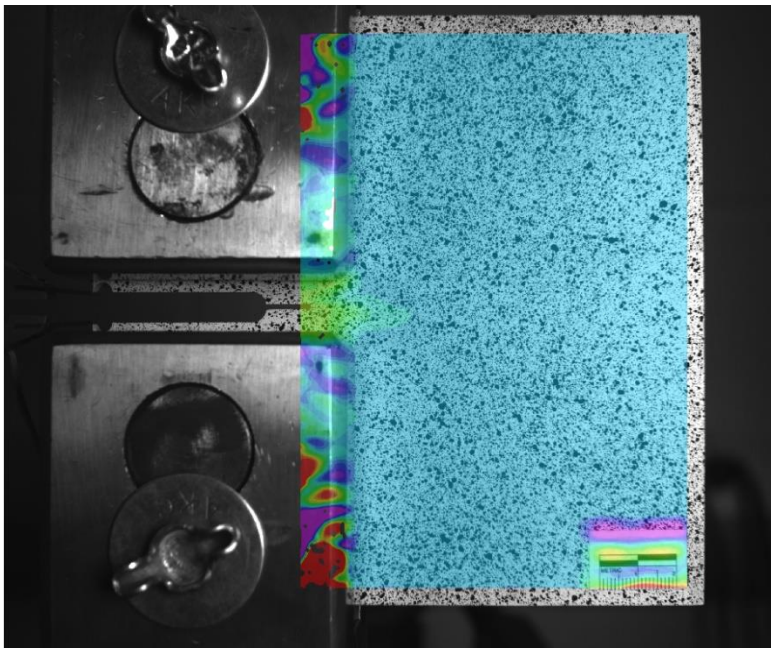

Figure A-41. Strain contours for C(T) specimen with 25.4 mm (1.0 in.) in-plane crack under loading case 1.

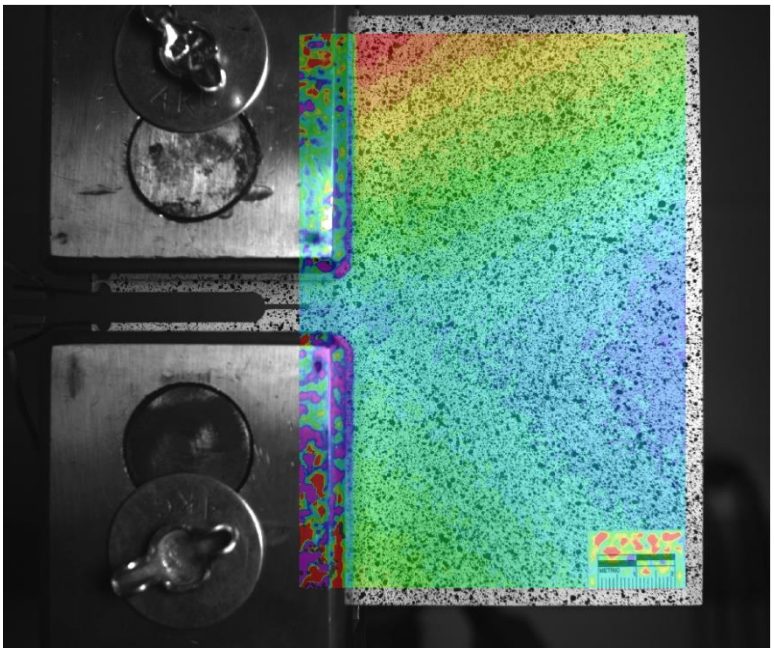

Figure A-42. Displacement contours for C(T) specimen with 25.4 mm (1.0 in.) in-plane crack under loading case 1.

Figure A-43. C(T) specimen with 25.4 mm (1.0 in.) in-plane crack under loading case 2.

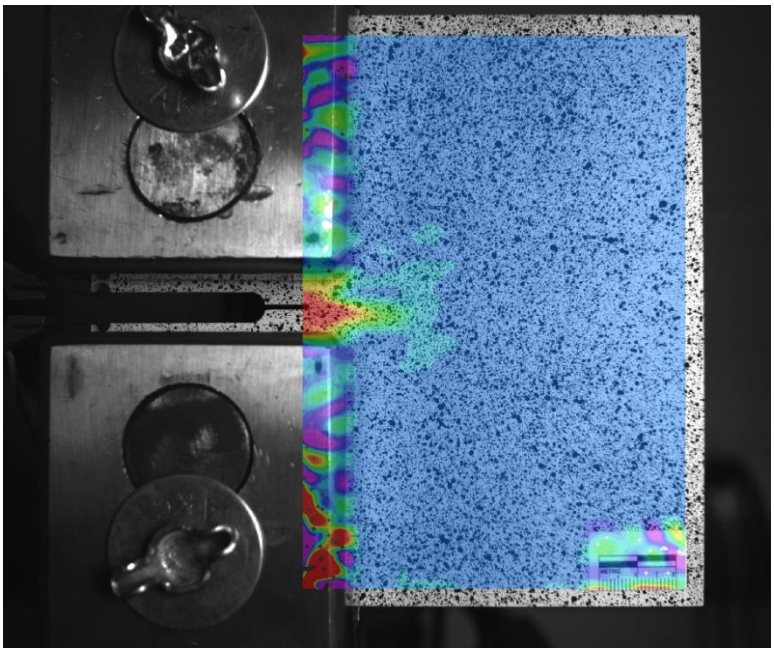

Figure A-44. Strain contours for C(T) specimen with 25.4 mm (1.0 in.) in-plane crack under loading case 2.

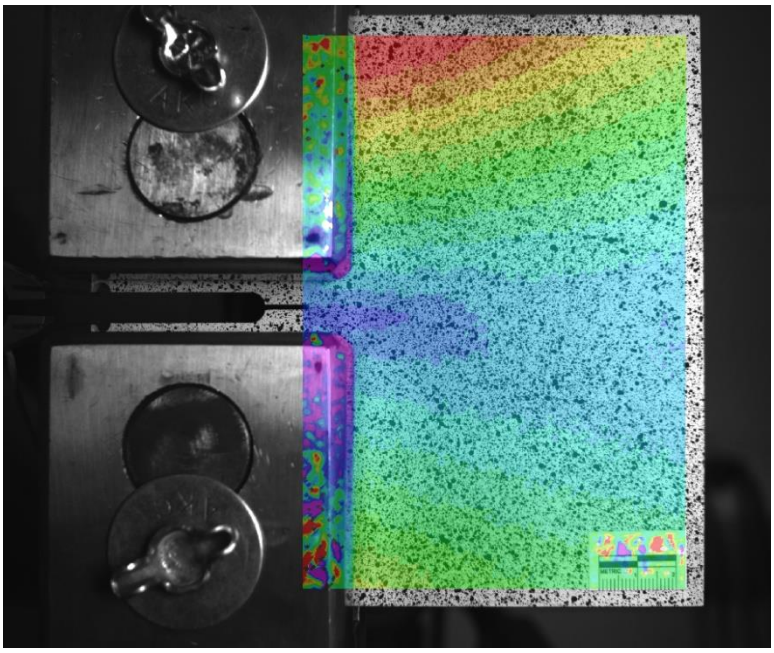

Figure A-45. Displacement contours for C(T) specimen with 25.4 mm (1.0 in.) in-plane crack under loading case 2.

Figure A-46. C(T) specimen with 25.4 mm (1.0 in.) in-plane crack under loading case 3.

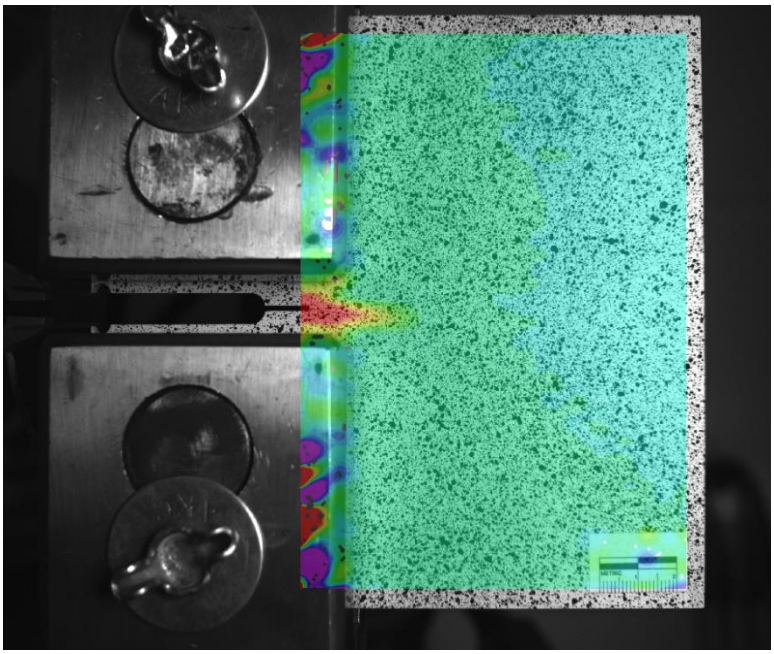

Figure A-47. Strain contours for C(T) specimen with 25.4 mm (1.0 in.) in-plane crack under loading case 3.

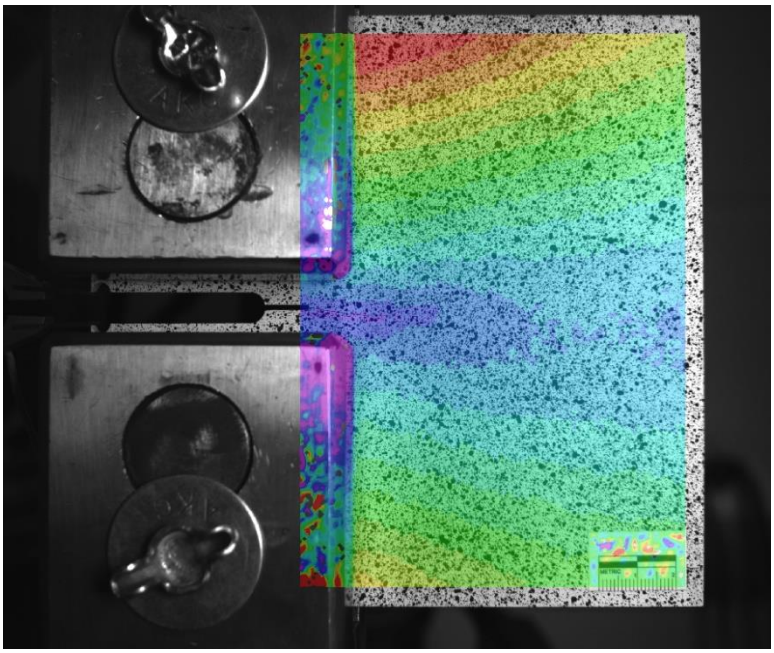

Figure A-48. Displacement contours for C(T) specimen with 25.4 mm (1.0 in.) in-plane crack under loading case 3.

Figure A-49. C(T) specimen with 25.4 mm (1.0 in.) in-plane crack under loading case 4.

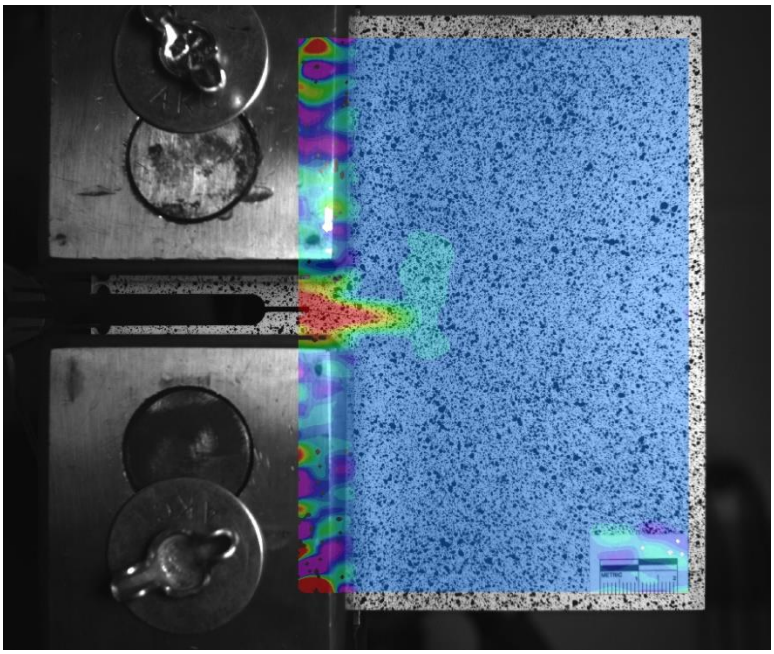

Figure A-50. Strain contours for C(T) specimen with 25.4 mm (1.0 in.) in-plane crack under loading case 4.

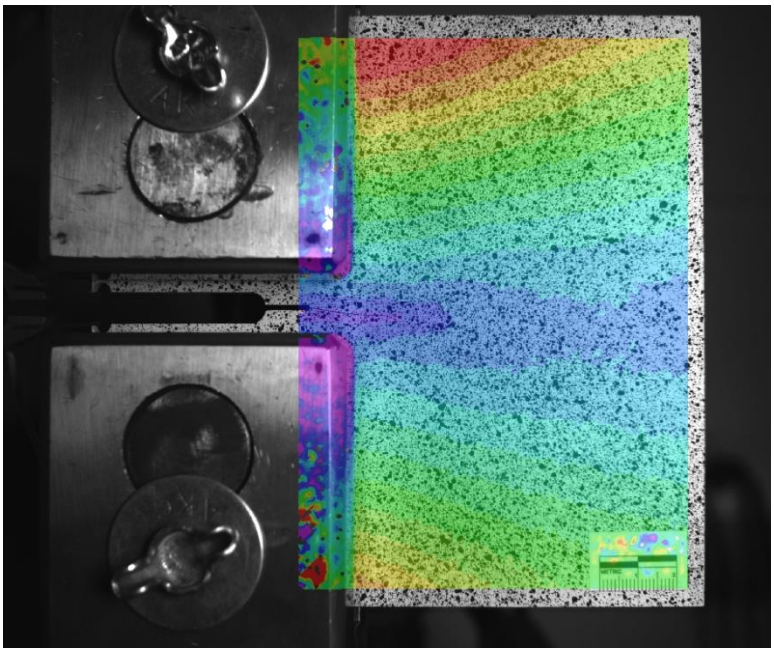

Figure A-51. Displacement contours for C(T) specimen with 25.4 mm (1.0 in.) in-plane crack under loading case 4.

Figure A-52. C(T) specimen with 25.4 mm (1.0 in.) in-plane crack under loading case 5.

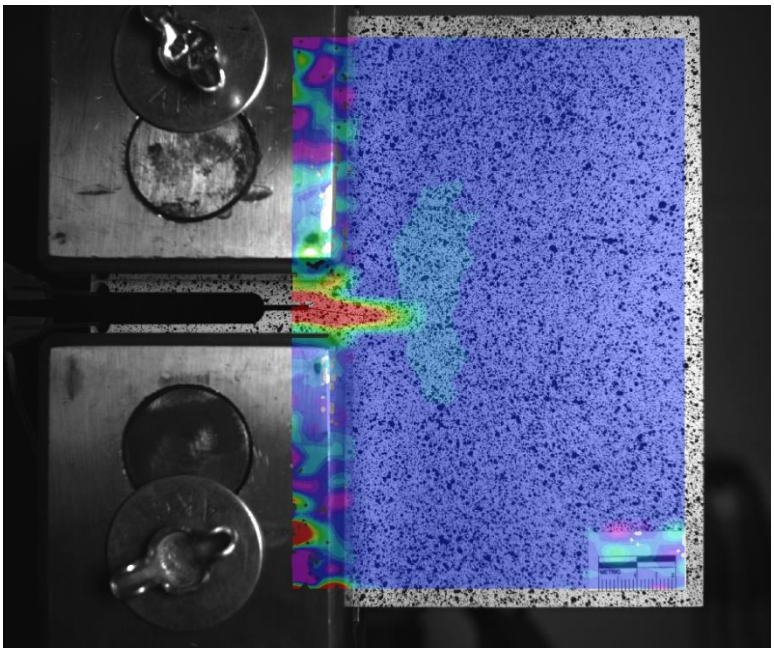

Figure A-53. Strain contours for C(T) specimen with 25.4 mm (1.0 in.) in-plane crack under loading case 5.

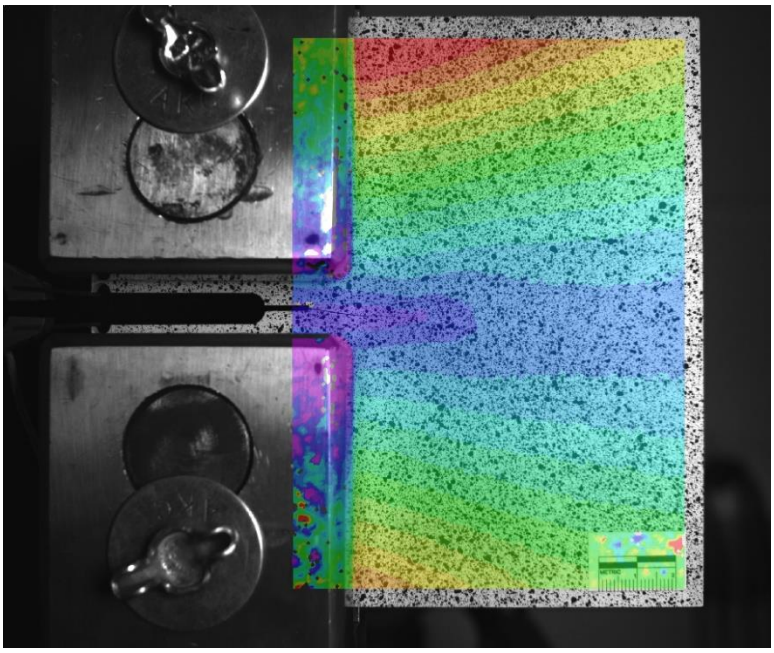

Figure A-54. Displacement contours for C(T) specimen with 25.4 mm (1.0 in.) in-plane crack under loading case 5.

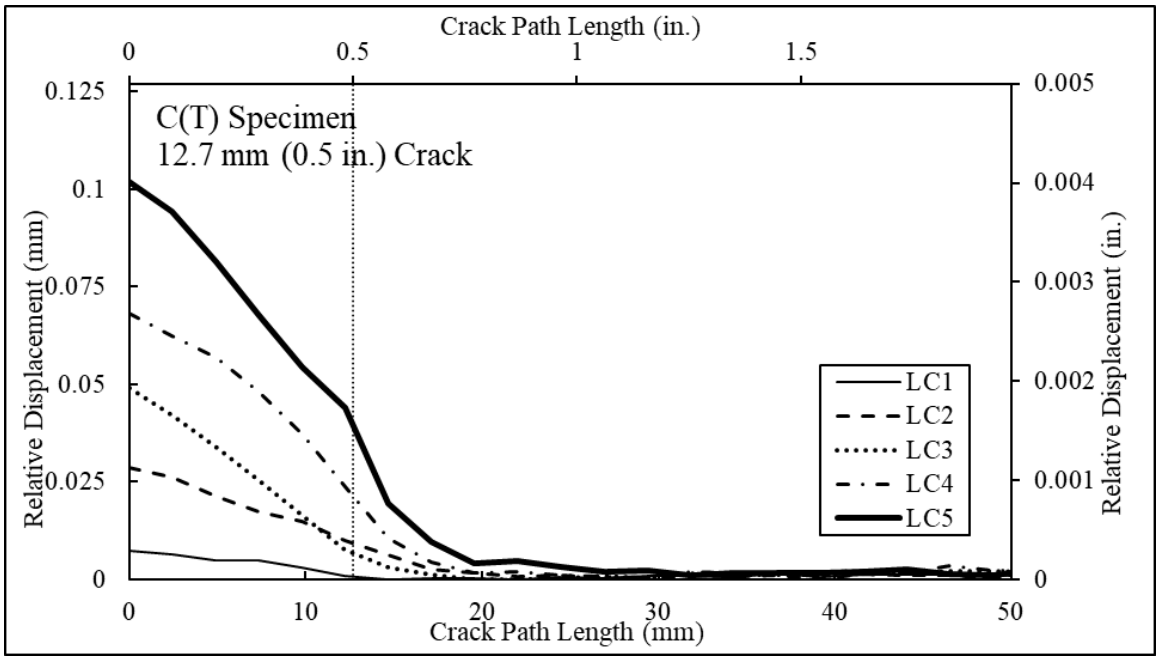

Figure A-55. Relative displacement along crack path for 12.7 mm (0.5 in.) cracked in-plane specimen.

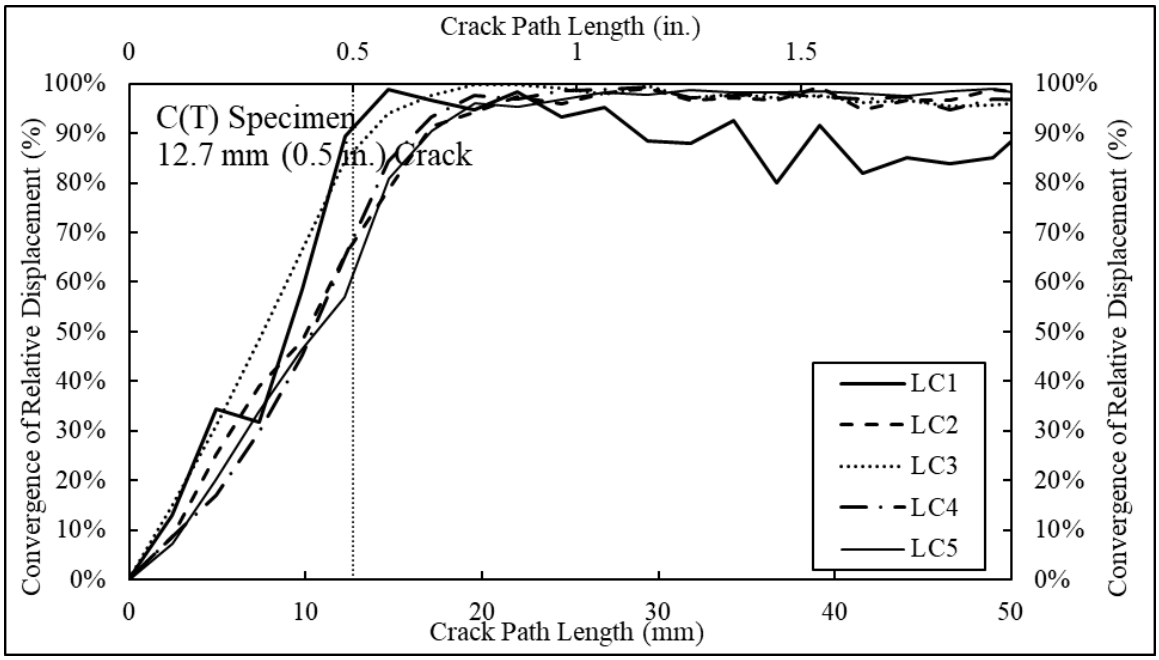

Figure A-56. Convergence of relative displacement for 12.7 mm (0.5 in.) cracked in-plane specimen.

Figure A-57. Unloaded C(T) specimen with 12.7 mm (0.5 in.) in-plane crack.

Figure A-58. C(T) specimen with 12.7 mm (0.5 in.) in-plane crack under loading case 1.

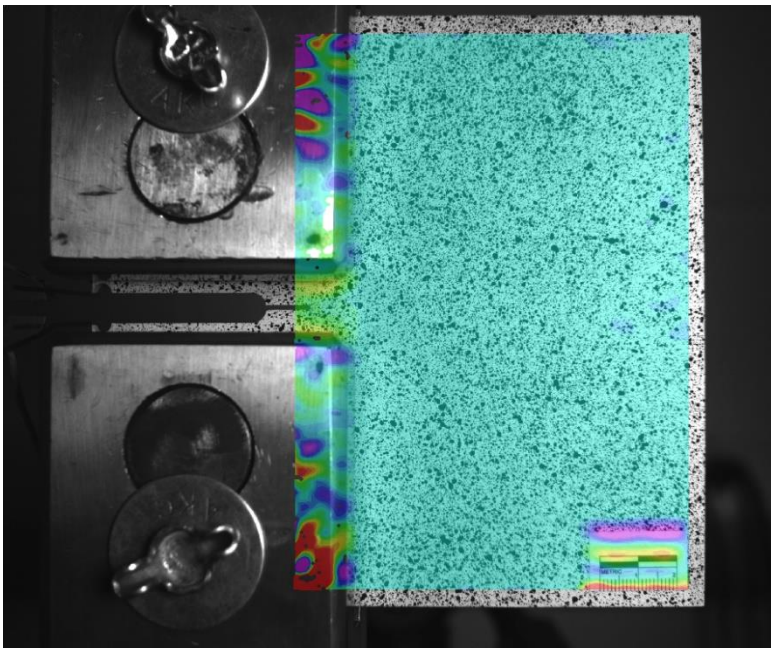

Figure A-59. Strain contours for C(T) specimen with 12.7 mm (0.5 in.) in-plane crack under loading case 1.

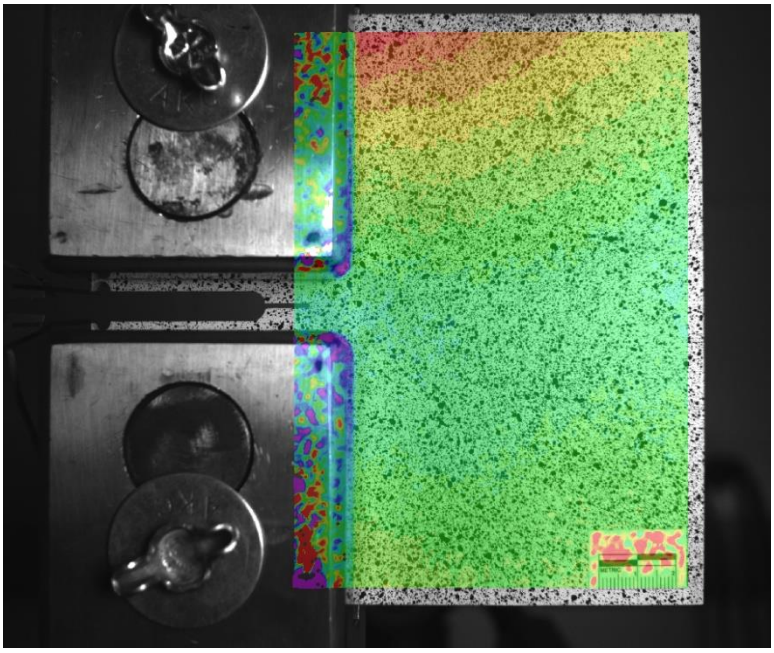

Figure A-60. Displacement contours for C(T) specimen with 12.7 mm (0.5 in.) in-plane crack under loading case 1.

Figure A-61. C(T) specimen with 12.7 mm (0.5 in.) in-plane crack under loading case 2.

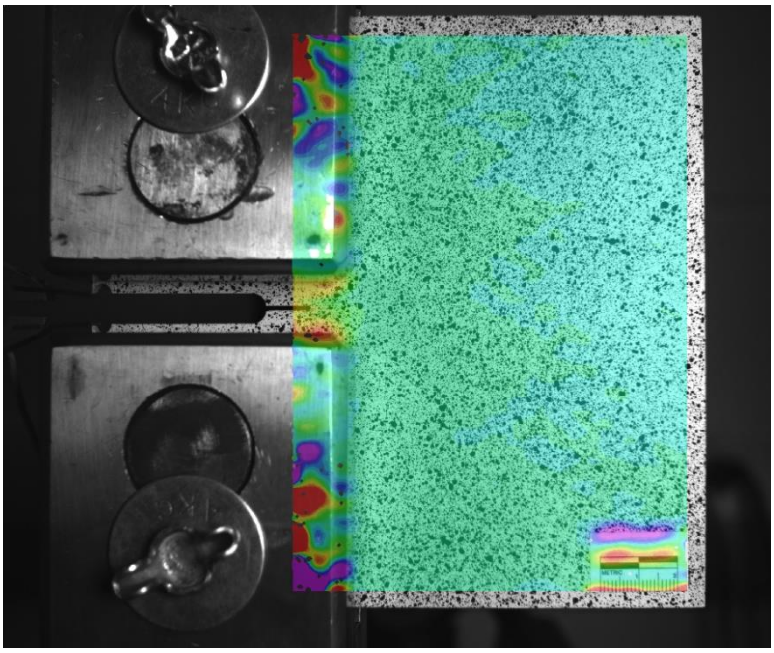

Figure A-62. Strain contours for C(T) specimen with 12.7 mm (0.5 in.) in-plane crack under loading case 2.

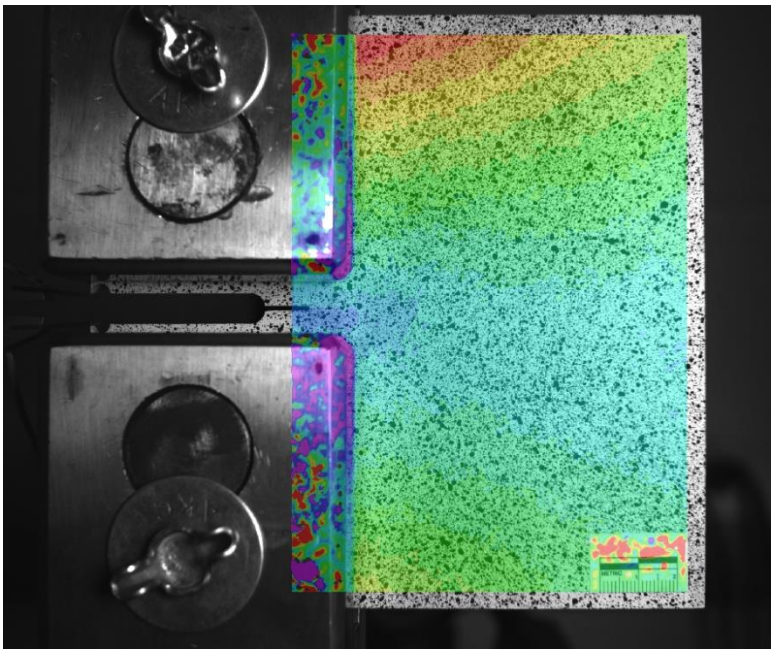

Figure A-63. Displacement contours for C(T) specimen with 12.7 mm (0.5 in.) in-plane crack under loading case 2.

Figure A-64. C(T) specimen with 12.7 mm (0.5 in.) in-plane crack under loading case 3.

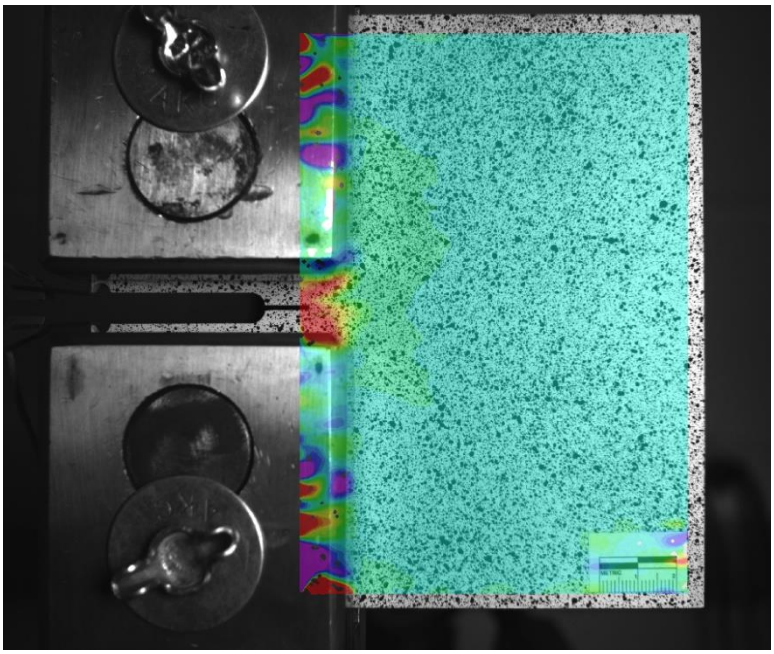

Figure A-65. Strain contours for C(T) specimen with 12.7 mm (0.5 in.) in-plane crack under loading case 3.

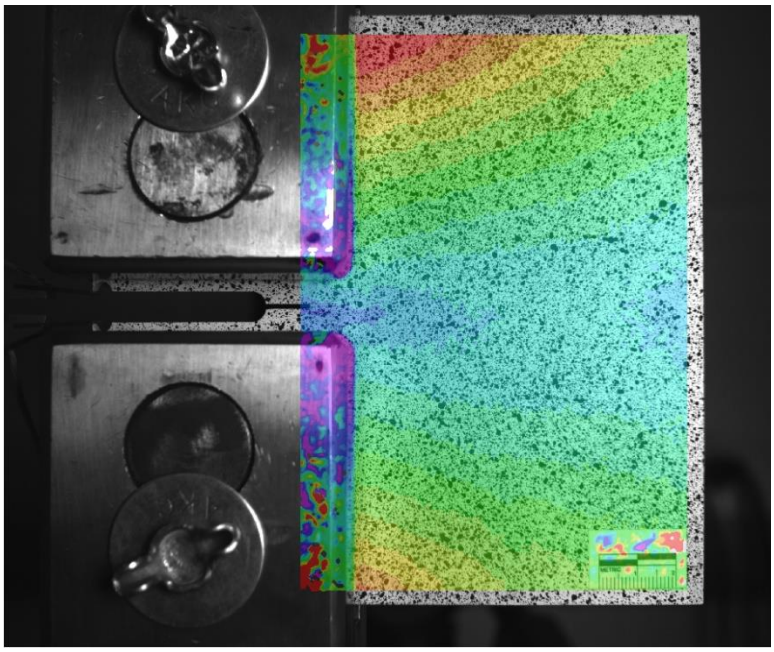

Figure A-66. Displacement contours for C(T) specimen with 12.7 mm (0.5 in.) in-plane crack under loading case 3.

Figure A-67. C(T) specimen with 12.7 mm (0.5 in.) in-plane crack under loading case 4.

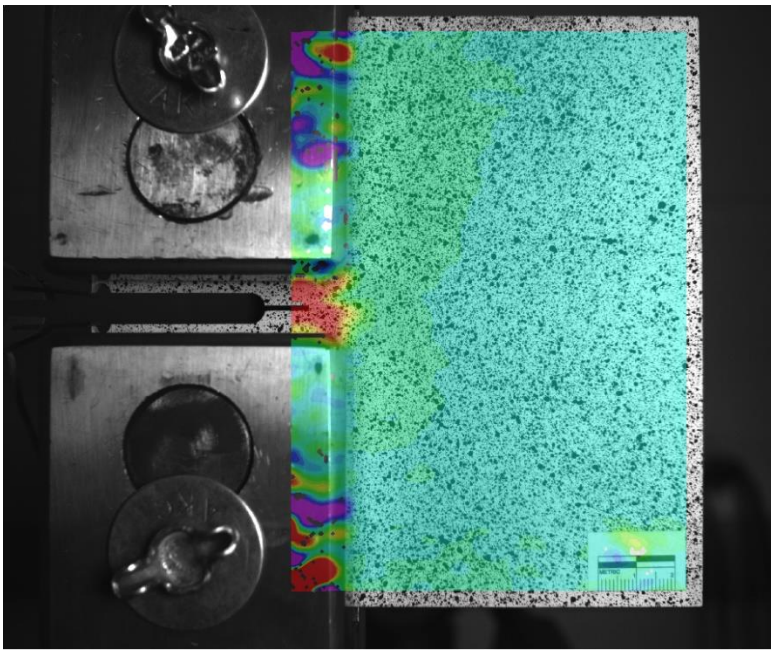

Figure A-68. Strain contours for C(T) specimen with 12.7 mm (0.5 in.) in-plane crack under loading case 4.

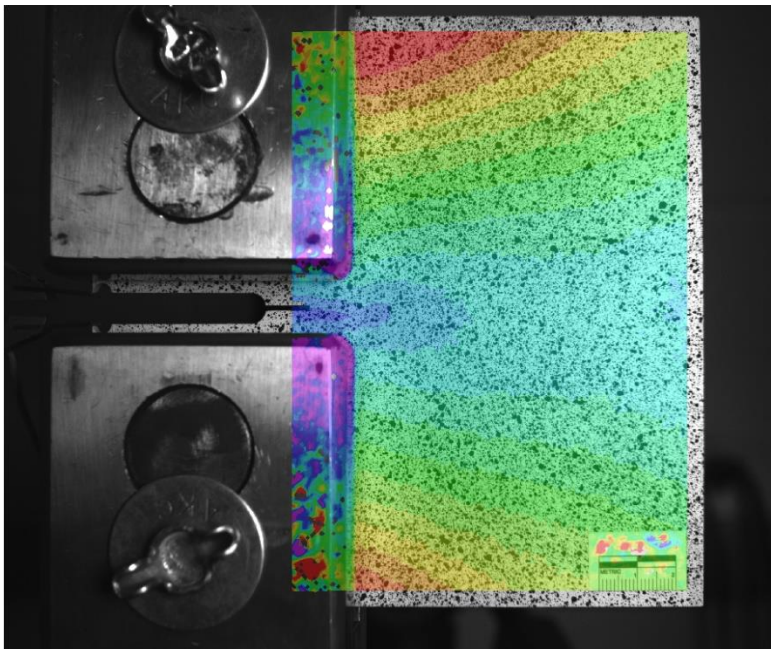

Figure A-69. Displacement contours for C(T) specimen with 12.7 mm (0.5 in.) in-plane crack under loading case 4.

Figure A-70. C(T) specimen with 12.7 mm (0.5 in.) in-plane crack under loading case 5.

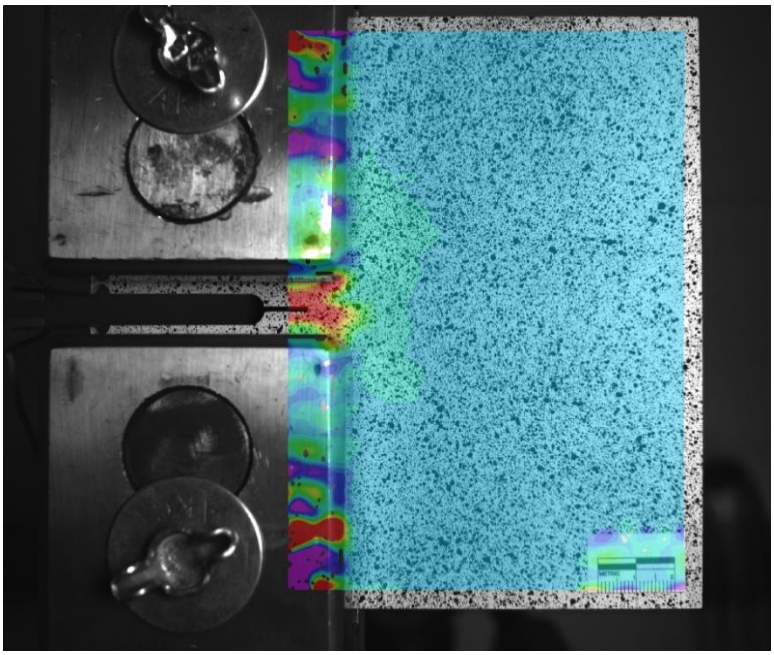

Figure A-71. Strain contours for C(T) specimen with 12.7 mm (0.5 in.) in-plane crack under loading case 5.

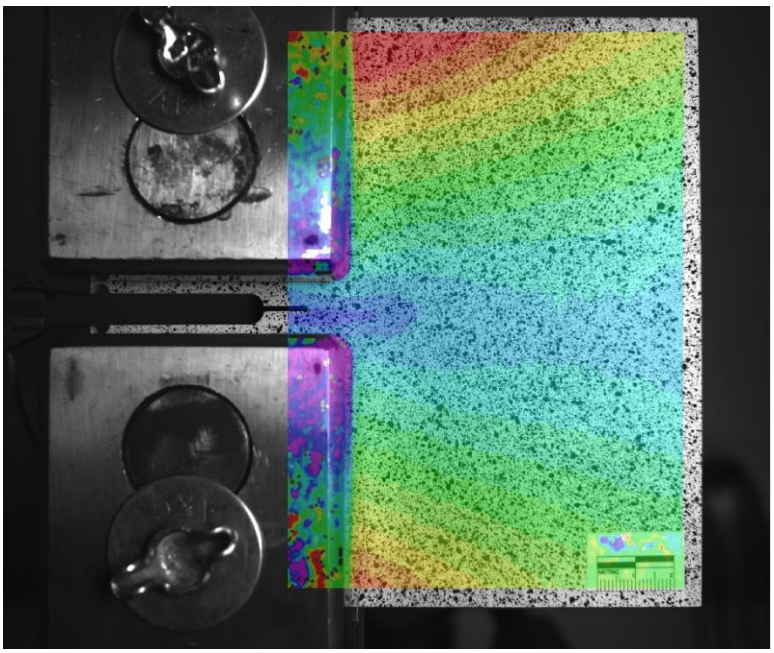

Figure A-72. Displacement contours for C(T) specimen with 12.7 mm (0.5 in.) in-plane crack under loading case 5.

Appendix B: Out-of-Plane Testing Data and Results

Shown below is a compilation of data for the out-of-plane test specimen. The data includes the following figures: relative displacement along the crack path, convergence of relative displacement, original image, strain contours for each load case overlaid on top of the original image, strain contours viewed in a 3D plot, and displacement contours for each load case overlaid on top of the original image.

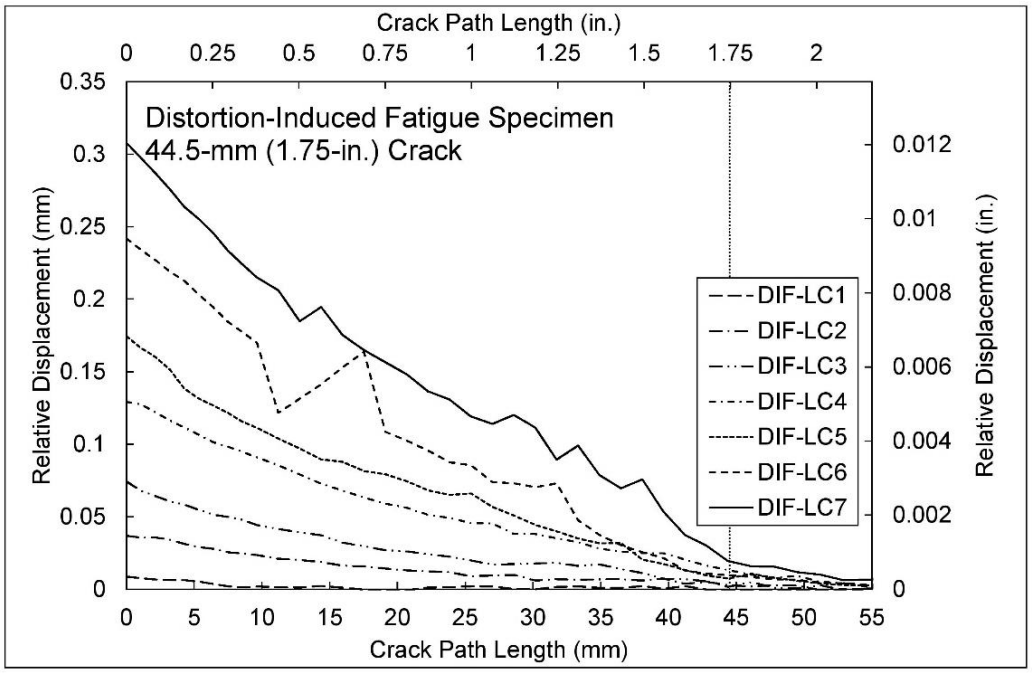

Figure B-1. Relative displacement along the crack path length for out-of-plane specimen.

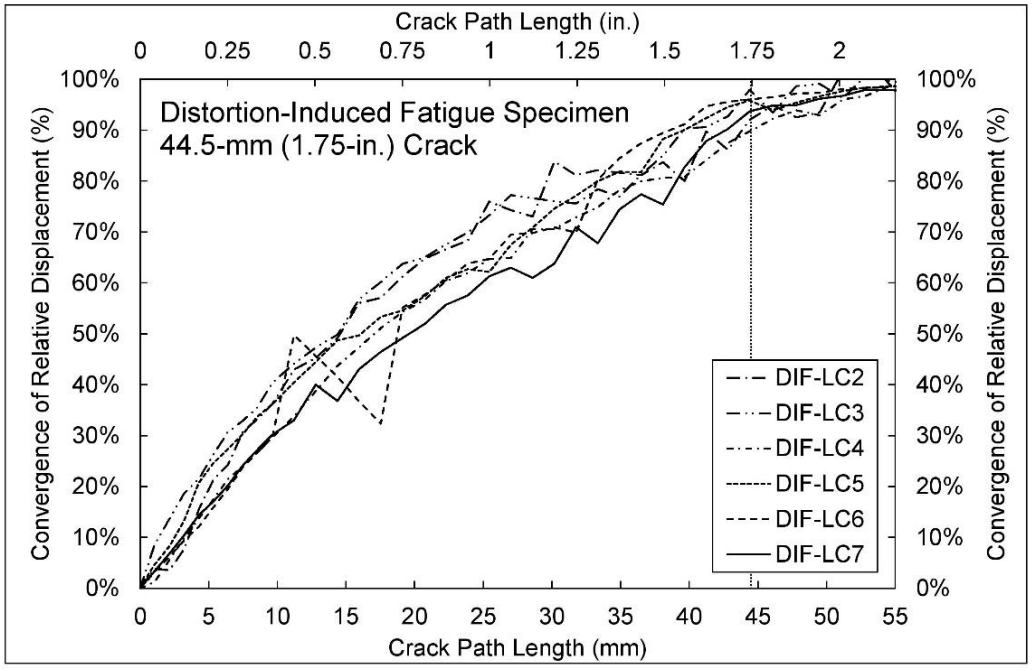

Figure B-2. Convergence of relative displacement for out-of-plane specimen.

Figure 0-3. Unloaded out-of-plane specimen with 44.5 mm (1.75 in.) crack.

Figure 0-4. Out-of-plane specimen under loading case 1.

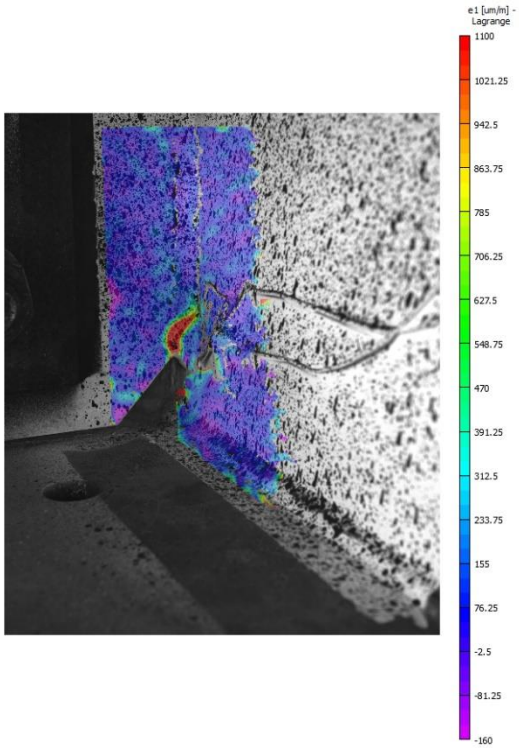

Figure 0-5. Strain contours for out-of-plane specimen under loading case 1.

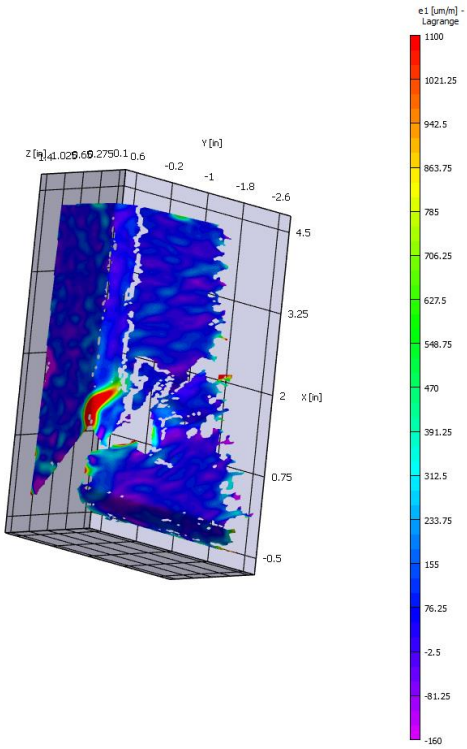

Figure 0-6. 3D graph of strain contours for out-of-plane specimen under loading case 1.

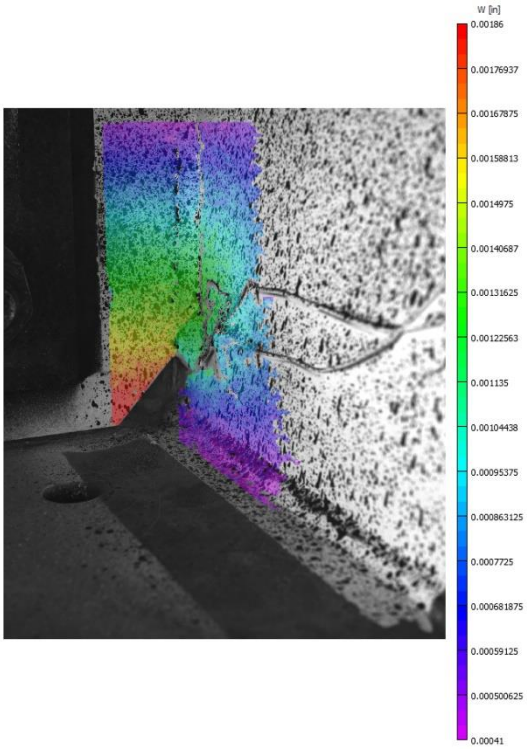

Figure 0-7. Displacement contours for out-of-plane specimen under loading case 1.

Figure 0-8. Out-of-plane specimen under loading case 2.

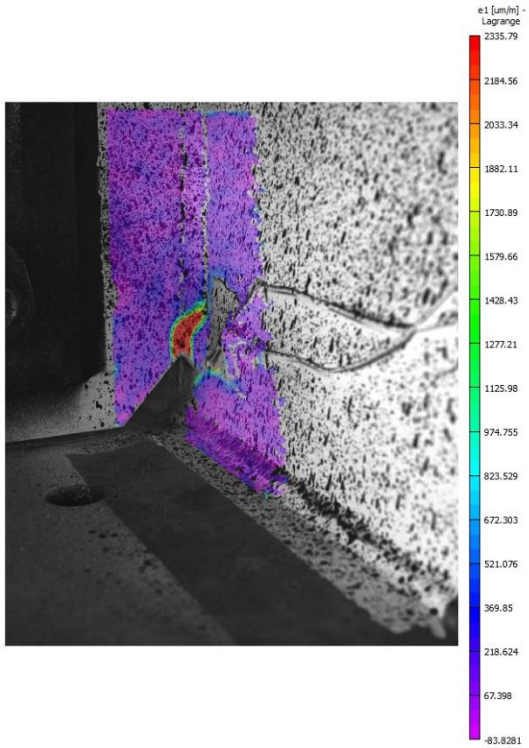

Figure 0-9. Strain contours for out-of-plane specimen under loading case 2.

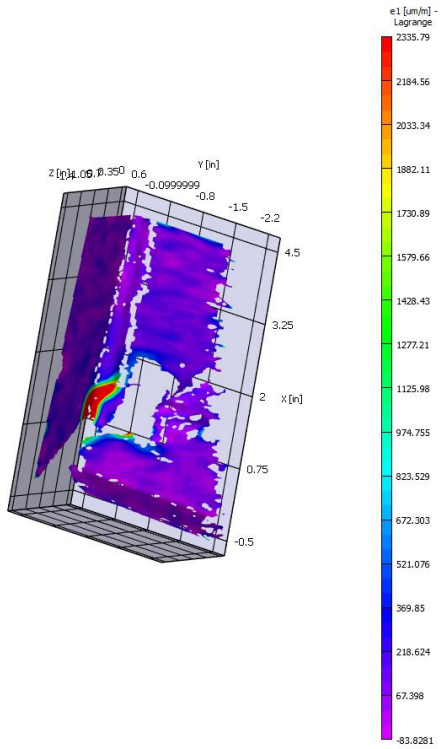

Figure 0-10. 3D graph of strain contours for out-of-plane specimen under loading case 2.

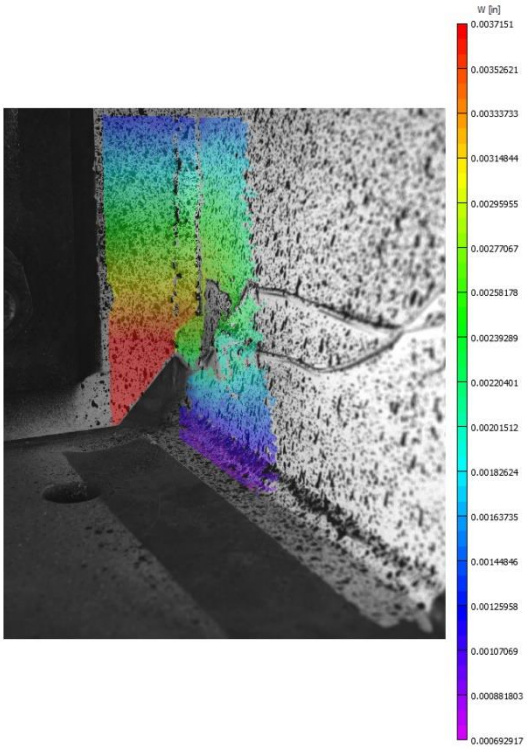

Figure 0-11. Displacement contours for out-of-plane specimen under loading case 2.

Figure 0-12. Out-of-plane specimen under loading case 3.

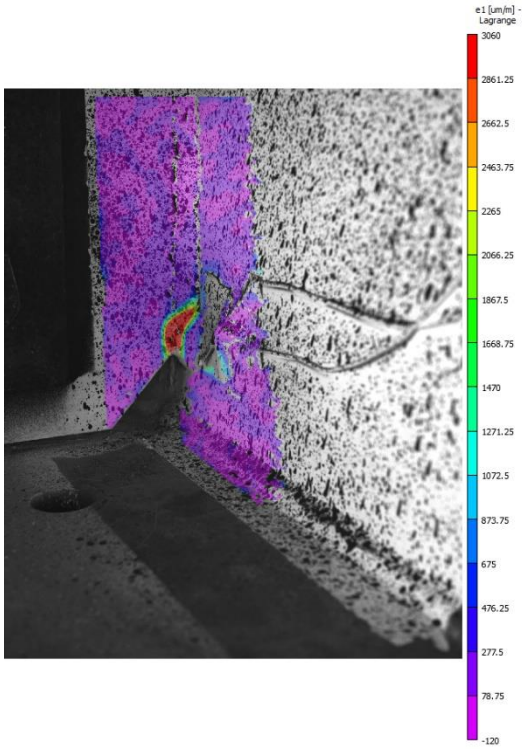

Figure 0-13. Strain contours for out-of-plane specimen under loading case 3.

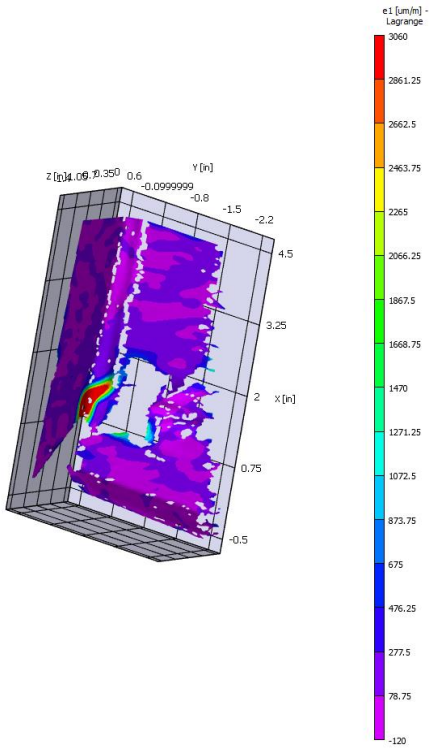

Figure 0-14. 3D graph of strain contours for out-of-plane specimen under loading case 3.

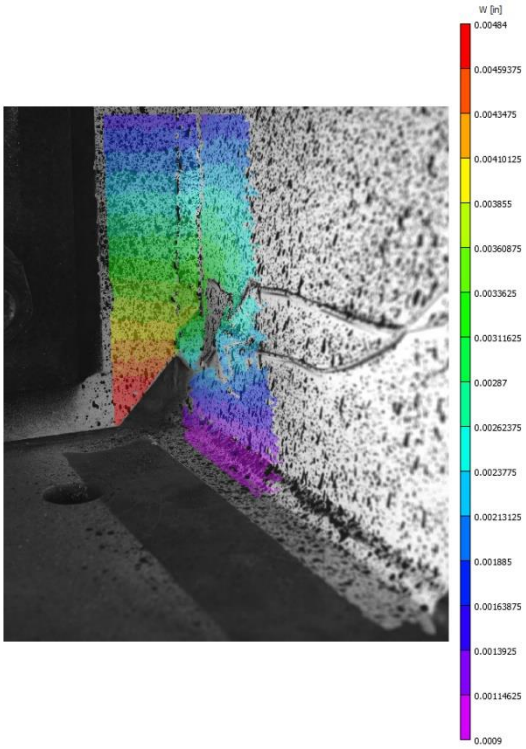

Figure 0-15. Displacement contours for out-of-plane specimen under loading case 3.

Figure 0-16. Out-of-plane specimen under loading case 4.

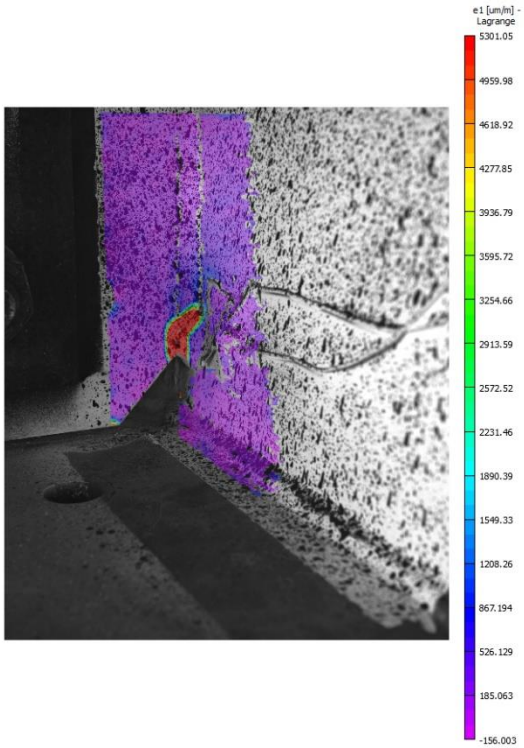

Figure 0-17. Strain contours for out-of-plane specimen under loading case 4.

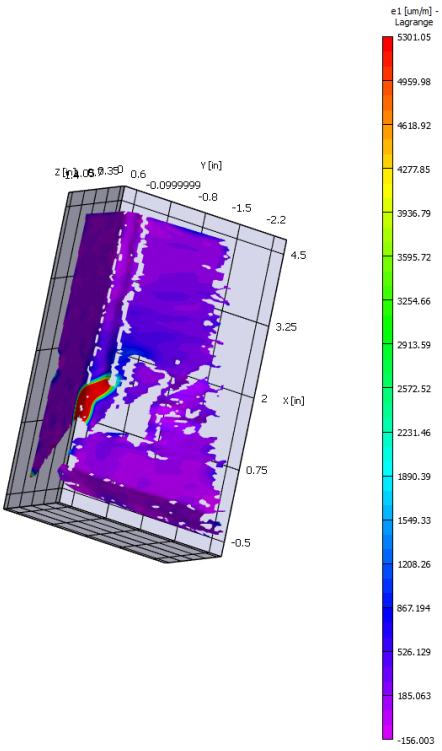

Figure 0-18. 3D graph of strain contours for out-of-plane specimen under loading case 4.

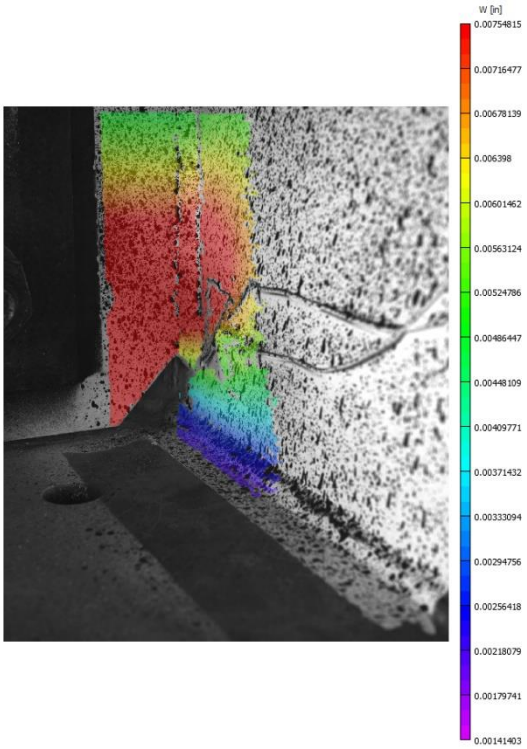

Figure 0-19. Displacement contours for out-of-plane specimen under loading case 4.

Figure 0-20. Out-of-plane specimen under loading case 5.

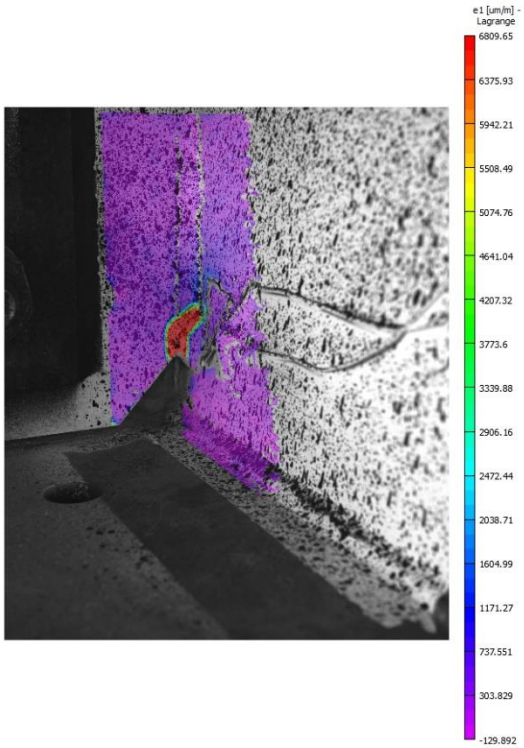

Figure 0-21. Strain contours for out-of-plane specimen under loading case 5.

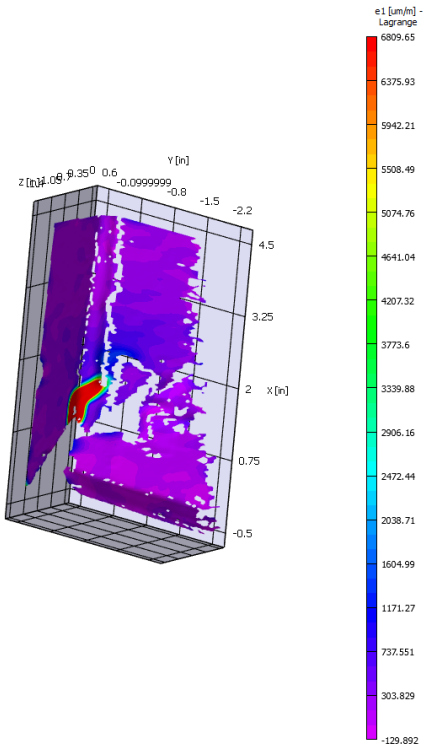

Figure 0-22. 3D graph of strain contours for out-of-plane specimen under loading case 5.

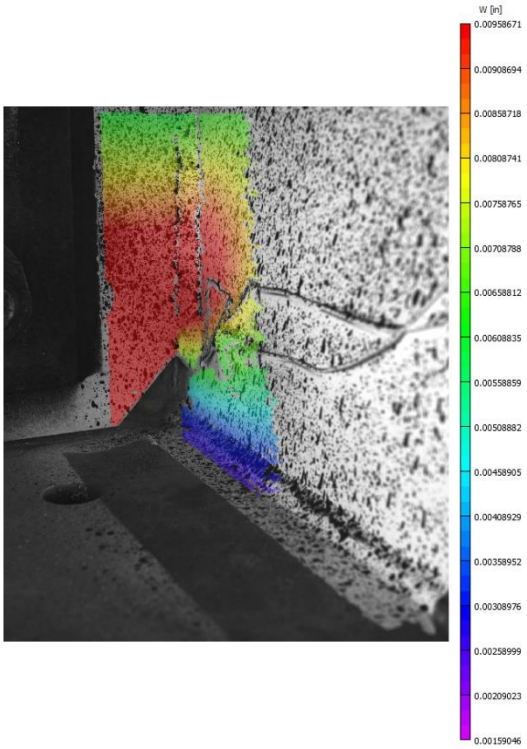

Figure 0-23. Displacement contours for out-of-plane specimen under loading case 5.

Figure 0-24. Out-of-plane specimen under loading case 6.

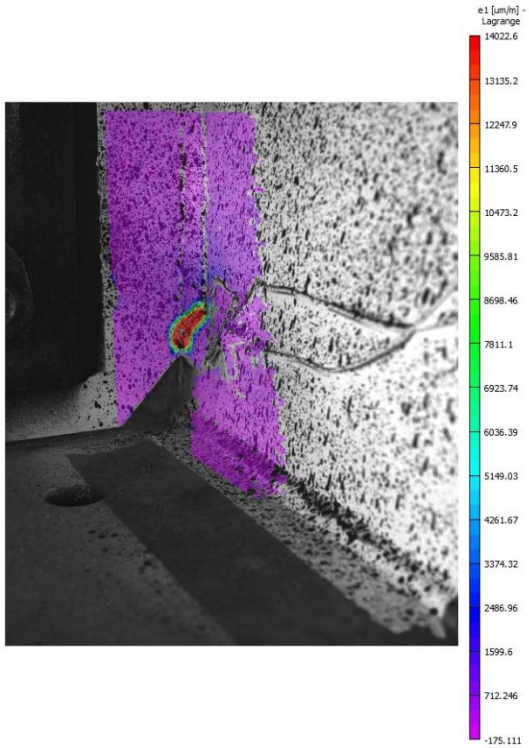

Figure 0-25. Strain contours for out-of-plane specimen under loading case 6.

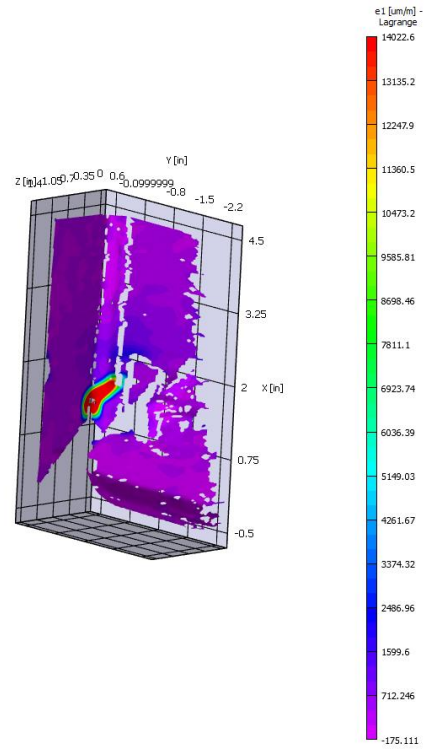

Figure 0-26. 3D graph of strain contours for out-of-plane specimen under loading case 6.

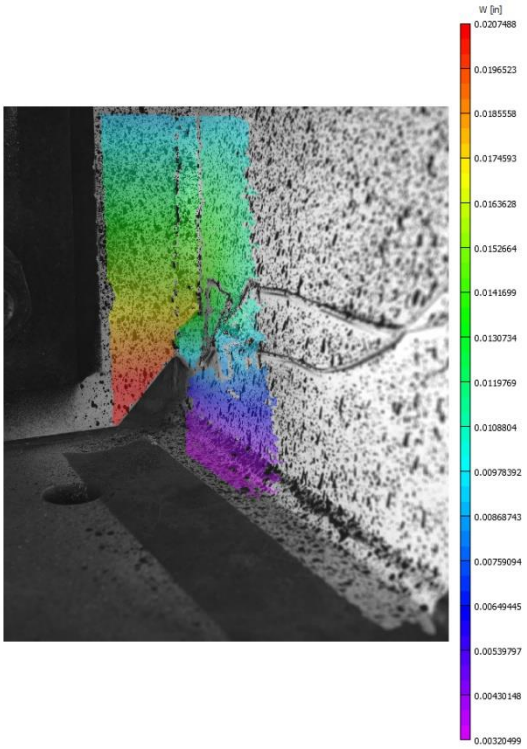

Figure 0-27. Displacement contours for out-of-plane specimen under loading case 6.

Figure 0-28. Out-of-plane specimen under loading case 7.

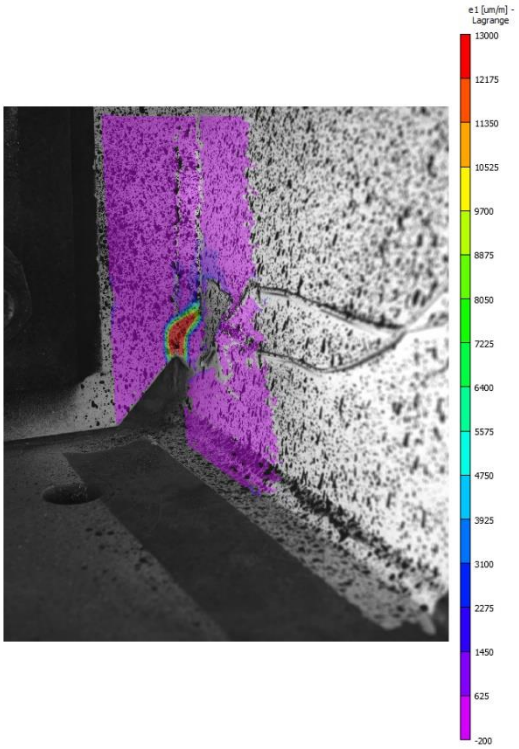

Figure 0-29. Strain contours for out-of-plane specimen under loading case 7.

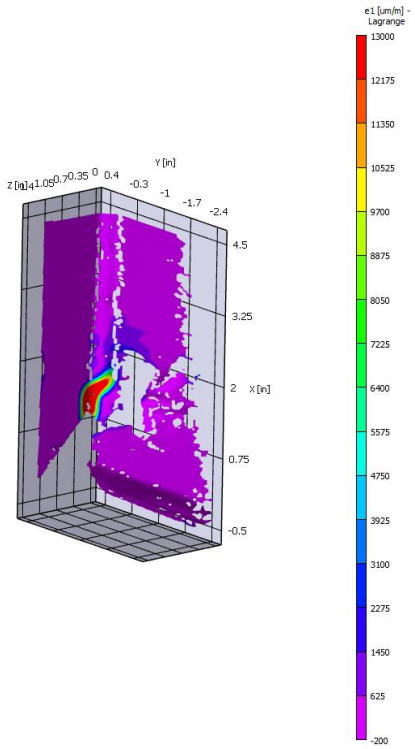

Figure 0-30. 3D graph of strain contours for out-of-plane specimen under loading case 7.

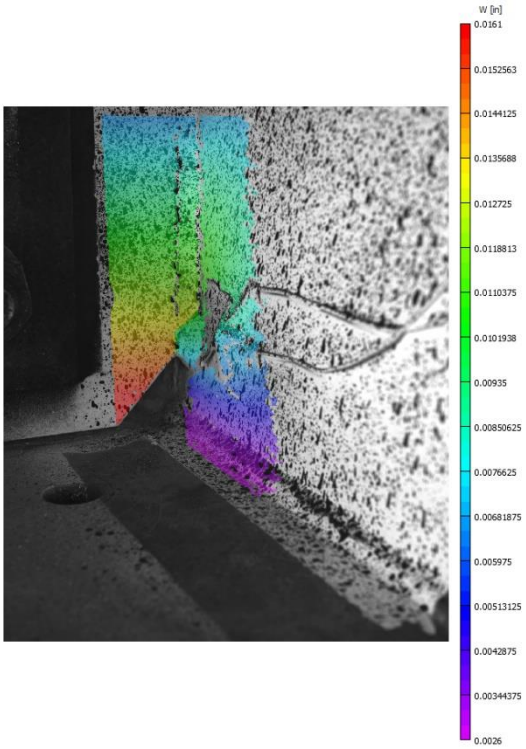

Figure 0-31. Displacement contours for out-of-plane specimen under loading case 7.